

Gone with the wind: Signatures of gas removal in environmentally perturbed galaxies

By

Taylah Kate Beard

A thesis submitted to Macquarie University
for the degree of Master of Research
Department of Physics and Astronomy
February 2020



MACQUARIE
University
SYDNEY • AUSTRALIA

Examiner's Copy

Except where acknowledged in the customary manner, the material presented in this thesis is, to the best of my knowledge, original and has not been submitted in whole or part for a degree in any university.

Taylah Kate Beard

Acknowledgements

I would like to express my heartfelt thanks to my supervisors Dr. Matt Owers and Dr. Ángel López-Sánchez for their keen interest and support which has helped me immensely through every stage of my thesis. Dr. Matt Owers, your timely advice, meticulous scrutiny, extensive knowledge and enthusiasm has guided and inspired me throughout this year. Dr. Ángel López-Sánchez, your insightful comments, constant encouragement and willingness to share your office has indeed made this year an enjoyable one.

My sincere thanks to the Department of Physics and Astronomy at Macquarie University for its support and wisdom, especially Dr. Joanne Dawson and Lisa Pesavento. I thank Macquarie University for monetary support by way of their scholarship.

With gratitude, I acknowledge the support and encouragement of all my family and friends. I especially wish to thank my Nanna and late Pa (who is always with me). Although they did not understand the intricacies of my research, they were always willing to listen. I am extremely thankful for my mother's unconditional belief in me, as well as her favourite quote which never fails to brighten my day:

"You is kind.

You is smart.

You is important." - The Help

Abstract

The knowledge of a galaxy's star formation history, both globally and in a resolved manner, provide key pieces of information for understanding galaxy formation and evolution. The KOALA integral field unit (IFU) and the AAOmega spectrograph on the Anglo-Australian Telescope (AAT) were used to follow up two galaxies within Abell 119 ($z = 0.0442$) which were previously investigated within the SAMI Galaxy Survey. The KOALA IFU provides a wider field of view of these galaxies when compared with the SAMI observations, allowing the search for signatures of environmental interactions which occur at large galactocentric distances, such as ionised tails of stripped gas. In both galaxies, 9011900084 and 9011900166, we observed one-sided extraplanar tails of ionised gas extending respectively ~ 16.1 kpc and ~ 6.1 kpc in projection off their stellar disk. The orientation of these tails in relation to the cluster centre inferred the galaxies direction of motion as towards apocentre from observed post-pericentre and pericentre positions, respectively. Line ratios measured in the tails indicate ionisation through non-SF LINER sources, unlike that observed in jellyfish galaxies. This thesis therefore supports a scenario where ram pressure stripping (RPS) is removing gas from galaxies as they traverse the cluster, leading to the ongoing quenching of star formation.

Contents

Acknowledgements	iii
Abstract	iv
Contents	v
List of Figures	vii
List of Tables	viii
1 Introduction	1
1.1 Properties of Galaxies	1
1.1.1 Morphology	1
1.2 Observational Evidence of Evolution	2
1.3 Mechanisms Driving Evolution	3
1.4 Manifestation of Environmentally Disturbed Galaxies	5
1.4.1 Post-starburst (‘k+a’) Galaxies	5
1.4.2 Green Valley Galaxies	6
1.4.3 Jellyfish Galaxies	6
1.5 Outline and aims of thesis	8
2 Observations and Data Reduction	10
2.1 The KOALA Instrument	10
2.2 Observations	10
2.3 Sample Selection	11
2.4 Data Reduction	12
2.4.1 Obtain the row-stacked spectra (RSS) files with 2dFDR	12
2.4.2 Obtain science-ready data cubes from RSS files using PyKOALA	13

3	Results and Analysis	19
3.1	Line Strength Measurements	19
3.1.1	Voronoi Binned Data	19
3.1.2	Continuum definition for individual spaxels	21
3.1.3	Emission line flux measurements	25
3.2	Results	27
3.2.1	Ionised gas properties of 9011900084 and 9011900166	27
3.2.2	Detailed Analysis of Individual Regions	30
4	Discussion	37
4.1	Evidence for Ram Pressure Stripping	37
4.2	Direction of Motion	38
4.3	Composition	38
5	Conclusion	41
5.1	Summary	41
5.2	Future Work	42
	References	44

List of Figures

1.1	Hubble Tuning Fork	2
1.2	Abell 119 SDSS Image	5
1.3	MUSE Jellyfish Galaxy	7
2.1	RSS to Data Cube	16
3.1	Voronoi Bin Output - 9011900084	20
3.2	Voronoi Bin Output - 9011900166	21
3.3	Central Spaxel of Galaxy 9011900084	22
3.4	Central Spaxel of Galaxy 9011900166	23
3.5	Flux Maps - 9011900084	26
3.6	Flux Maps - 9011900166	27
3.7	Multiple Subsections - 9011900084	28
3.8	Multiple Subsections - 9011900166	29
3.9	Region and Flux Ratio Maps - 9011900084	31
3.10	Region and Flux Maps - 9011900166	32
3.11	BPT Region Diagrams	34
4.1	Galaxy Direction of Motion	40

List of Tables

2.1	Parameters of Galaxies	11
2.2	Summary of AAT observations using KOALA	18
2.3	Summary of AAT archive observations	18
3.1	Emission lines considered in this study	25
3.2	9011900084 region values for Flux, V_{gas} and σ_{gas}	35
3.3	9011900166 region values for Flux, V_{gas} and σ_{gas}	36

1

Introduction

One of the main challenges in modern astrophysics is to achieve a complete understanding of how galaxies evolve over time. Knowledge of a galaxy's star formation (SF) history, both globally and in a resolved manner, are key to understanding galaxy formation and evolution. One approach to advancing our understanding is to study galaxies during a singular extreme state of evolution. By focusing on galaxies caught in the act of transformation, it may be possible to identify the dominant mechanism/s responsible for galaxy transformation.

1.1 Properties of Galaxies

1.1.1 Morphology

A galaxy is a gravitationally bound system, comprising of: stars, gas, dust, stellar remnants and dark matter. Each galaxy can be classified according to their morphology when observed at visual wavelengths using the system developed by Edwin Hubble in the 1920's (Hubble, 1926). Figure 1.1 visually demonstrates the galaxy classifications, which are subdivided into three main categories: Elliptical galaxies (E), Spiral Galaxies (S/SB), and Lenticular galaxies (S0).

Elliptical galaxies display a smooth, spheroidal structure. Each galaxy is categorised with a numerical index ranging from 0 to 7 indicating their ellipticity; E0 galaxies are visually spherical, where E7 galaxies are highly elliptical. Elliptical galaxies are generally devoid of ongoing SF, contain minimal gas and dust, and their stellar component is dominated by old, passively evolving populations.

Spiral galaxies contain thin disks with spiral arms extending from the central region which is engulfed in a halo of stars. There are two main branches of spiral galaxies; those in which the spiral arms extend from a central bulge (classic spirals: S), and those where the arms extend from a central

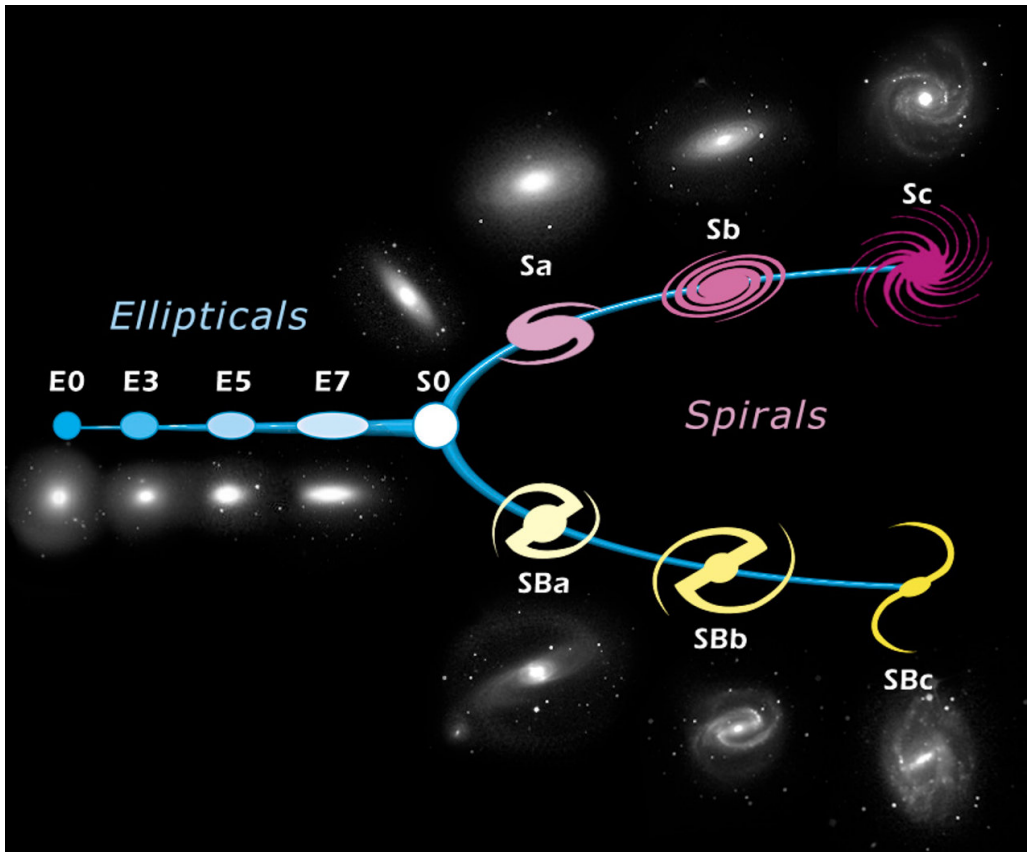


FIGURE 1.1: Edwin Hubble's galaxy morphological classification scheme. Based on their morphology, galaxies are divided into three main classes: ellipticals (left), lenticular galaxies (S0) and spirals (right). Spiral galaxies are then divided into two subcategories: classic spirals (top, S) and barred spirals (bottom, SB). (Credit: <https://www.spacetelescope.org>).

bar structure (barred spirals: SB). Galaxies within each branch are then separated into three classes: *a*, *b*, and *c*. This distinction is based on the compactness of the spiral arms, the size of the central bulge region, and the overall thickness of the arms due to gas and dust. Spiral galaxies have an abundance of gas and dust, resulting in the intermediate to young stellar components. Lenticular galaxies represent an intermediate class between elliptical and spiral galaxies. They contain a disk and nuclear bulge similar to spiral galaxies, however have no visual gas, dust or spiral arms like spiral galaxies.

1.2 Observational Evidence of Evolution

There are many lines of evidence indicating that galaxy properties change with time, which is potentially due to the influences of the surrounding environment. Cosmic SF history observations by Madau (1995) indicates that the SF rate of galaxies decline as they move towards the present epoch. Furthermore, observations such as the 'Butcher-Oemler effect', (Butcher & Oemler, 1978, 1984) reveal that at high redshifts there is a higher fraction of blue, SF galaxies in the cores of rich galaxy clusters

compared to the low redshift galaxies, indicating the rapid evolution of the SF properties of cluster galaxies. The morphology-density relation reveals the strong correlation between galaxy morphology and density (Dressler, 1980). Dense environments within the cores of clusters are observed to be dominated by passive elliptical and lenticular galaxies, while lower density field environments are dominated by SF spiral galaxies. It is assumed that clusters and other dense regions grow by accreting matter from lower density regions which are rich in spirals (Poggianti et al., 2009). This infers that environment-related processes are at play, but are unable to identify the dominant mechanism. Many mechanisms exist that may be responsible for the alteration in galaxy morphology and SF rates, which are described below.

1.3 Mechanisms Driving Evolution

The evolution of galaxies depend upon both external and intrinsic events, occurring throughout a galaxies lifetime. External events include: galaxy mergers, tidal interactions, harassment, ram-pressure, viscous stripping, thermal evaporation, and starvation (Boselli & Gavazzi, 2006). An Active Galactic Nuclei (AGN, Radovich et al. 2019) outflow is an example of an intrinsic event, which primarily drives outflows of ionised gas into the surrounding environment which trigger SF and possibly feeds the AGN (Bing et al., 2019; Harrison et al., 2014). AGN feedback is one of the primary mechanisms thought responsible for quenching SF in massive galaxies (Croton et al., 2006).

Galaxy mergers and tidal interactions (TI) are strong gravitational interactions which alter a galaxy's structure along with triggering SF (Barnes & Hernquist, 1996). There are multiple forms of galaxy merger events, the most common being the galaxy fly-by where two or more galaxies approach close enough such that each galaxy influences the gravitational field of the other galaxy (Kauffmann et al., 1993). These interactions alter the galaxy's morphology through the potential creation of structures such as disk warps, bars or tidal tails (Toomre & Toomre, 1972). Interactions involving high-speed fly-by encounters with other galaxies are referred to as galaxy harassment or TI (Moore et al., 1996; Byrd & Valtonen, 1990; Toomre & Toomre, 1972), with extended emission regions of ionised gas being produced between the interacting galaxies. These gravitationally perturbed regions trigger central SF resulting in the depletion of gas reserves within the galaxy, causing the quenching of SF, along with producing tail and bridge structures within spiral galaxies.

'Ram-pressure stripping' (RPS, Gunn & Gott 1972) is a process whereby an interaction with the intracluster medium (ICM) strips away the galaxy's gas when a galaxy passes through the dense ICM

within the cluster core. The effects of RPS depend on the properties of both the galaxy and ICM as well as the relative velocity, with a timescale equivalent to one cluster crossing time or a few Gyrs ($\sim 10^9$ years) (Gunn & Gott, 1972). Low redshift studies of galaxies within the Coma cluster by Gunn & Gott (1972) have shown evidence of stripping material from the galaxy into the cluster environment. Tail structures appearing in the opposite direction to which the galaxy is moving, and SF within these regions, result in the formation of jellyfish galaxies (Merluzzi et al., 2013; Fumagalli et al., 2014). RPS events have been studied around the Virgo and Coma clusters (Smith et al., 2010; Yagi et al., 2010; Poggianti et al., 2017b; Boselli et al., 2018b), as well as in other nearby systems, such as the Shapley Concentration (Merluzzi et al., 2013, 2016) or Abell 3627 (Sun et al., 2007).

The starvation of a galaxy occurs due to the loss of hot gas reservoirs located in the galaxies outer extremities. SF in these galaxies may only continue through using the cooler gas remaining in the galaxy, resulting in the unavoidable quenching of the galaxy due to all gas and dust being completely exhausted (Larson et al., 1980). This results in the galaxies metallicity levels increasing rapidly, due to the lack of dilution available from the ceased inflow of external gas (Trussler et al., 2019).

The knowledge of a galaxy's SF history, both globally and in a resolved manner, provide key pieces of information for understanding galaxy formation and evolution. Recent studies (Boselli et al., 2019; Cora et al., 2018; Merluzzi et al., 2016; Ramatsoku et al., 2019) have investigated how surrounding environments affect the evolution process of a galaxy, however, how this is achieved is still an open question. There are specific morphological features that assist with the identification of galaxies that are being affected by a particular process, such as those investigated by Poggianti et al. (2019); Merluzzi et al. (2016). Therefore, investigating individual galaxies undergoing a single external interaction assists to further understand to what extent the environment plays a role in the evolution of galaxies.

At the present epoch, galaxy clusters are the largest structures in the universe that have had time to virialize, containing up to a few thousand galaxies within a radius of $R_{200} \sim 3$ Mpc (Abell et al., 1989), where R_{200} represents the radius where the average mass density is 200 times the critical density of the universe. This places galaxies in the same region in the sky, making clusters a useful tool to study galaxy evolution. Within these regions the environmental interactions are most prominent and presents an ideal location to investigate the physical processes responsible for galaxy transformation. This is shown in Figure 1.2 with galaxy cluster Abell 119.



FIGURE 1.2: This SDSS survey image shows the galaxies within the galaxy cluster Abell 119. North is towards the top of the page and West is towards the right.

1.4 Manifestation of Environmentally Disturbed Galaxies

Galaxies have been identified, outside the traditional classifications shown in Figure 1.1, which represent galaxies in the process of quenching. These include galaxies known as post-starburst ($'k+a'$), green valley and jellyfish galaxies.

1.4.1 Post-starburst ($'k+a'$) Galaxies

Post-starburst ($'k+a'$) galaxies, also referred to as $'E+A'$ galaxies, are defined by their strong Balmer absorption lines and absence of emission line features (Dressler & Gunn, 1983; Vergani et al., 2018). This is indicative of galaxies experiencing intense SF within the last billion years, however, currently contain minimal ongoing SF. For this evolution to occur, the violent removal or exhaustion of galaxy gas is required. This may occur due to mechanisms such as galaxy mergers or RPS (Zabludoff et al., 1996). Past studies, such as by Snyder et al. (2011), reveal that although these mechanisms assist with rapid removal of gas, these processes alone do not suffice in triggering a $'k+a'$ phase.

1.4.2 Green Valley Galaxies

The ‘green valley’ (GV) represents a region in the $NUV - r$ (Wyder et al., 2007) colour magnitude diagram (CMD) which lies between the SF sequence (‘blue cloud’, BC) and passive sequence (‘red sequence’, RS) (Salim, 2014). The galaxies which are transitioning between the BC and RS regions are referred to as green valley galaxies (GVGs), and inhabit the GV region. These CMD regions were selected due to ultraviolet (UV) emission being sensitive to recent SF predominately within the BC region, while r-band observations aid in the identification of stellar mass regions.

Galaxies within the GV are predominately bulge-dominated, disk galaxies which presently experience SF within their disks which is observed through UV imaging. Faber et al. (2007) hypothesised the transition of galaxies from the BC to RS, due to the observed increase of RS galaxies with time. There are multiple theories posed regarding this transition. Trayford et al. (2016) utilised the EAGLE cosmological hydrodynamical simulation to reveal the characteristic time scale for galaxies to cross the GV to be $\sim 2\text{Gyr}$, independent of all quenching mechanism. Through studying UV observation, Fang et al. (2012) proposed the static nature of the GV on the CMD. Instead of the previously believed galaxy transition from the BC to RS, Fang et al. (2012) identifies that galaxies appeared to occupy the same location on the CMD as they evolve over time. Therefore, it was posed that it is the GV which moves slowly towards the lower SF rate section of the CMD over time.

It has also been investigated that galaxies may not always follow the transition from BC through the GV to RS, instead moving from the RS to the GV due to external environmental events such as (Thilker et al., 2010). Coenda et al. (2018) states that there are many possible scenarios which could lead to the creation of GVGs, however, external quenching sources play a major role in the evolution of galaxies. The extent to which each mechanisms plays a role depends upon the location of the galaxy in relation to the galaxy cluster itself.

1.4.3 Jellyfish Galaxies

Jellyfish galaxies are excellent signposts of ICM-ISM ram-pressure interactions. As RPS acts upon the gas from within the stellar disk, due to interactions with the ICM, starbursts are triggered in-situ in the stripped gas tail (Poggianti et al., 2019). These SF features enabled the identification of tails in optical/UV imaging, which otherwise would have require deep radio or IFU observations. SF is observed taking place in stripped tails, as seen in Figure 1.3 where massive, luminous SF clumps within the tail region characterise SF within extreme environments (Vulcani et al., 2019). These tail

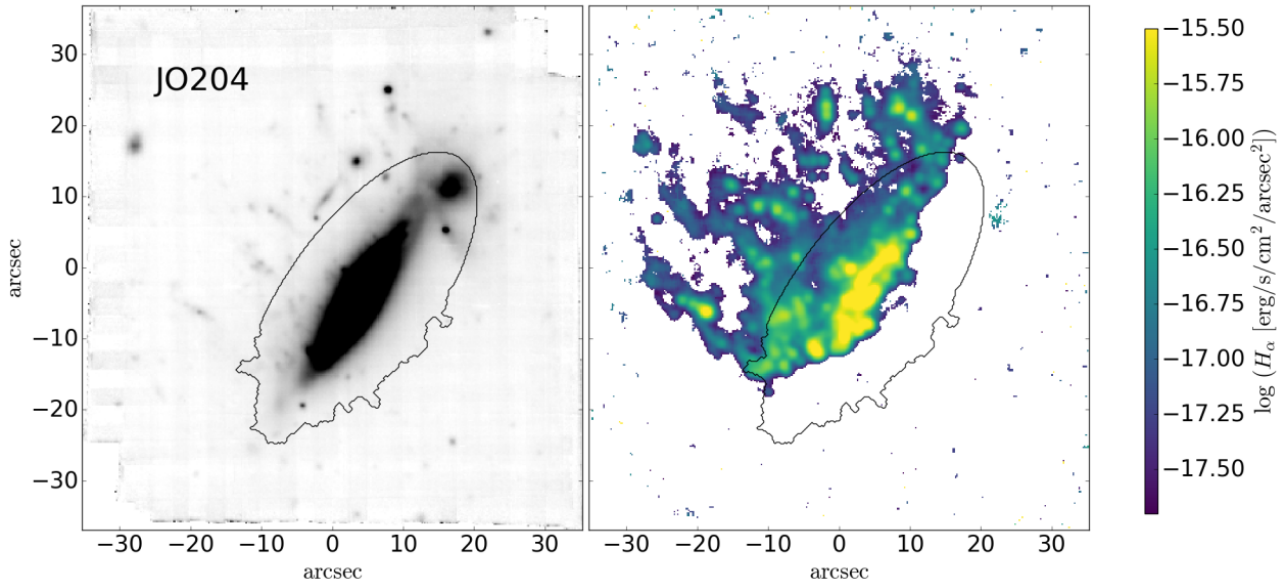


FIGURE 1.3: This figure contains MUSE white image (left) and the respective H_α flux map (right) for galaxy JO204. The black contours show the stellar contours which represents the ‘galaxy boundary’. This image was taken from Poggianti et al. (2019).

features extend in the opposite direction to which the galaxy is moving through the dense central region of its respective cluster.

Investigation into the gas tail extension direction in relation to the centre of cluster, such as within the Coma cluster by Smith et al. (2010), led to determining the galaxy’s direction of motion in the plane of the sky. Smith et al. (2010) found that 11/13 galaxies investigated contained tails oriented away from the cluster centre, indicating these galaxies are on their first fall into the cluster centre.

Through investigating galaxies undergoing transformation in the Shapley super-cluster, Merluzzi et al. (2016) determines that RPS can take place in very different environments, from cluster cores to cluster outskirts and from rich clusters to poor ones, affecting galaxies of various masses numerous ways. The GASP¹ survey (Poggianti et al., 2017b) highlights the open questions surrounding how RPS affects the SF activity of galaxies. It was hypothesised within Poggianti et al. (2017c) that the RPS process could be triggering the active galactic nucleus (AGN, Radovich et al. 2019). This is supported by the fact that $\approx 86\%$ jellyfish galaxies within the GASP survey contain an AGN (Poggianti et al., 2017a). This could be accounted for through the ISM interacting with the non-rotating ICM resulting in the loss of angular momentum, forcing material into the central region of the galaxy (George et al., 2019).

¹<https://web.oapd.inaf.it/gasp/>

1.5 Outline and aims of thesis

This work investigates the potential environment-related mechanisms that are quenching galaxies. Galaxies rarely evolve with a singular physical mechanism, rather they experience a combination of various physical mechanisms randomly throughout their lifetime. Certain circumstances lead to single mechanisms being dominant within a galaxy, resulting in structures forming mostly due to this singular mechanism. Through investigating these mechanisms, evolutionary models can be restricted in order to gain a clearer picture of a galaxy's history.

This study investigates two galaxies, 9011900084 and 9011900166, upon their first fall into the central region of the galaxy cluster Abell 119 (Owers et al., 2019) as shown in Figure 1.2. These galaxies were selected from the SAMI Galaxy Survey (Bryant et al., 2015) based on their resolved spectroscopic properties, indicating their SF is being quenched from the outside-in (Owers et al., 2019). This is a signpost of environment-driven ‘quenching’ of SF. A detailed environmental analysis led Owers et al. (2019) to conclude that these galaxies are on their first fall into the high-density central region of the galaxy cluster. In conjunction with the outside-in quenching signature, Owers et al. (2019) suggested that these galaxies are being affected by RPS. This leads to the cessation of SF on the first passage through the cluster. There were several open questions on the interpretation around the SAMI galaxies this thesis aims to address (Owers et al., 2019), listed as follows:

1. **The evidence for RPS was inferred indirectly through the investigation of $EW(H\alpha)$ emission features within the central region of galaxies. Direct evidence in the form of one-sided tails of gas was hinted at in a subset of galaxies, however due to the limited SAMI field of view (FoV) these could not be directly investigated. Therefore, through the wider FoV provided by KOALA, an investigation into stripped ionised gas tails and the environmental mechanism responsible for these features is performed.**
2. **Owers et al. (2019) was unable to ascertain the future evolution of the SAMI $H\delta$ -strong galaxies (HDSGs). Galaxies were observed with SF still present at their centres, however, direction of motion through the cluster was unable to be ascertained. Due to this uncertainty, questions arise such as: do these galaxies maintain some central SF as they approach apocentre, or are they completely stripped as they proceed through pericentre? Understanding this is key to understanding the future evolution of SF activity in these galaxies, and therefore the timescales for quenching. Identifying the orientation of galaxy tails with respect to pericentre within this thesis will place constraints upon the evolution**

of SF within galaxies.

3. **Additionally, this thesis attempts to understand the ionising source for any emission features within the observed gas tails. Through exploring HII-like regions conclusions may be drawn as to if the galaxies investigated harbour ongoing star formation in their tails, such as that observed in jellyfish galaxies.**

The aims allow a stringent test of the RPS hypothesis put forward by Owers et al. (2019), as well as to further our understanding of these galaxies and their interaction with the environment. The wide field of view (FoV) provided by the KOALA Integral field unit (IFU: Zhelem et al. 2014; Ellis et al. 2012) instrument on the Anglo-Australian Telescope (AAT: Zhelem et al. 2014) will be used to search for tails of ionised gas (Boselli et al., 2016, 2018b) which are only present at distances larger than the plane of the galaxy's stellar disk. Past analysis presented by Owers et al. (2019) utilised the SAMI Galaxy Survey (Croom et al., 2012) which only probed the central region of the galaxies. Therefore, data obtained from KOALA will provide a wider field of view in order to observe the galaxy's surrounding environment and allow for the detection of these one-sided, extraplanar tails of ionised gas. Therefore, analysing galaxies using the KOALA data enables the exploration of environmental interactions, providing a test of the hypothesis put forward in Owers et al. (2019) that RPS is responsible for the quenching within the investigated galaxies.

Observations and Data Reduction

2.1 The KOALA Instrument

KOALA (Kilofibre Optical AAT Lenslet Array, Ellis et al., 2012) is a wide-field, high efficiency, integral field unit (IFU) mounted at the f/8 Cassegrain focus of the Anglo-Australian Telescope (AAT). KOALA utilises 1000 micro-lenses to cover the field of view (FoV) of either 15.3 arcsec x 28.3 arcsec (0.7" sampling) or 27.4 arcsec x 50.6 arcsec (1.25" sampling) depending on the magnification used (Zhelem et al., 2014). This enables a much larger area of a galaxy to be covered compared to that used by the SAMI galaxy survey, where only the central 15 arcsec diameter region was observed (Allen et al., 2015; Bryant et al., 2015). KOALA feeds the AAOmega spectrograph (Saunders et al., 2004; Smith et al., 2004; Sharp et al., 2006) via a 31m fibre run. AAOmega is a double beam spectrograph with selectable wavelength coverage and resolution that is achieved via interchangeable gratings.

2.2 Observations

The IFU data presented within this thesis were taken from two main sets of observations. The primary target galaxies, 9011900084 and 9011900166, were observed at the AAT using KOALA+AAOmega on 2016 October 24th and 25th, respectively, along with the calibration data, as seen in Table 2.2. Supplementary dark and detector flat calibration files were obtained from the AAT archive¹ which were observed within a month previous to those of the primary observations. These supplementary calibration files were selected due to their similarity with our KOALA+AAOmega data, containing the same grating and wavelength range. Observation types, run quantity, exposure time and seeing conditions are summarised in Table 2.3.

¹<https://datacentral.org.au/>

Name	R.A. (J2000)	Dec. (J2000)	z	R	Velocity
	[deg.]	[deg.]		[kpc.]	[km/s]
9011900084	14.162282	-1.293969	0.0503	324.2	1755.6
9011900166	14.237376	-1.211027	0.0500	550.5	1668.5
Abell 119 Centre	14.067150	-1.255370	0.0442	-	-

TABLE 2.1: Parameters of galaxies 9011900084 and 9011900166 within galaxy cluster Abell 119, as well as the cluster centre (Owers et al., 2019). The projected distance (R) is from the cluster centre and the listed velocity is measured with respect to the cluster redshift.

For this project we used the 580V and 1000R gratings for the blue and the red arm of AAOmega, respectively. This configuration gives a rest-frame wavelength coverage from $\sim 3600\text{--}5400\text{ \AA}$ in the blue arm and $\sim 5800\text{--}7200\text{ \AA}$ in the red arm. This provided the instrument spectral resolution of $\sigma_{\text{BLUE}} = 1.19\text{ \AA}$ in the blue arm and $\sigma_{\text{RED}} = 0.70\text{ \AA}$ in the red.

For each galaxy, multiple pointings were observed using the wide-field mode of KOALA, giving $1.25''$ sampling and a $27.4'' \times 50.6''$ FoV. Each pointing was offset slightly from the previous pointing to help reconstruct the 3D cubes during the data processing and to minimise the impact of the few (14) KOALA dead spaxels. This dither pattern produces data cubes with a slightly larger FoV. For the galaxy 9011900166, one additional pointing was offset by $10''$ to the west in the direction of the cluster centre.

We obtained bias, dark, and detector flat images for calibration purposes. The flat fielding and the throughput correction was achieved using twilight sky flats. Observations of a CuAr lamp (‘arc frames’) were used to acquire the wavelength calibration. We also obtained offset sky frames in order to perform a proper sky subtraction. Spectrophotometric standard stars were used for obtaining the absolute flux calibration and get the telluric correction.

2.3 Sample Selection

Abell 119 was identified by Abell (1958) and contains 578 spectroscopically confirmed cluster members (Owers et al., 2017) within 4 Mpc of the cluster centre located at R.A. = 14.067150 degrees, dec. = -1.255370 degrees (J2000). Within this thesis we investigate two galaxies, 9011900084 and 9011900166, which were selected due to their potential for experiencing RPS (Owers et al., 2019). Parameters for these galaxies and the cluster centre are listed within Table 2.1. For calculating the distances we assumed a standard Λ CDM cosmology with $\Omega_m = 0.3$, $\Omega_\Lambda = 0.7$ and a Hubble constant

$H_0 = 70 \text{ km s}^{-1} \text{ Mpc}^{-1}$. The velocities of the two galaxies relative to their redshift are $v_{pec} = 1755.6$ and 1668.5 km s^{-1} for 9011900084 and 9011900166, respectively.

2.4 Data Reduction

This section describes the procedure used to produce fully calibrated data cubes from the individual, uncalibrated raw exposures collected at the AAT (Tables 2.2 and 2.3), as described in Section 2.2. Preliminary reduction, using the 2dFDR package to obtain the row-stacked spectra (RSS), is described in Section 2.4.1 and the procedure for producing fully combined, flux-calibrated data cubes using PyKOALA (López-Sánchez et al. in prep) is described in Section 2.4.2. The process of reducing, calibrating, and creating data cubes have to be performed for both the blue and red arm spectra separately.

2.4.1 Obtain the row-stacked spectra (RSS) files with 2dFDR

Initial steps in the data reduction procedure are performed using the 2dFDR software (Croom et al., 2004; Sharp & Birchall, 2010), with the aim of producing calibrated row-stacked spectra in preparation for the cubing process described in Section 2.4.2. The steps followed are similar to those performed for the SAMI Galaxy Survey and outlined in detail in Sharp et al. (2015). An overview of the procedure required to produce the RSS is given below. The following steps are applied in order to extract the object, offset sky, calibration stars, and twilight flat frames for each arm of the dual-beam AAOmega instrument.

1. Bias subtraction: This is achieved through fitting a polynomial to the over scan region such that the overall bias is subtracted from these frames. Any residual artefacts in the bias and dark current are then removed through subtracting combined high signal to noise bias and dark frames.
2. Detector flats are used to correct for pixel-to-pixel variations on the CCD. This is performed by removing large-scale features from defocused flat frames, leaving only pixel-to-pixel variations. These processed frames are used for the pixel-to-pixel correction. Large-scale wavelength-dependent and spatial flat field corrections will be described in Section 2.4.2.
3. Cosmic rays are high-energy protons that can leave high-intensity features when they hit the CCD during an exposure. These high-intensity regions are identified in 2dFDR using a modified

version of the cosmic ray rejection by Laplacian edge detection (LACOSMIC) routine (van Dokkum, 2001; Husemann et al., 2012). The input parameters for the LACOSMIC routine were tuned to produce reliable results for both the blue- and red CCDs without masking sky and emission lines. Pixels associated with cosmic ray streaks are masked.

4. Tramline mapping and fibre profile definition: Tramline mapping traces the flux in the fibres, identifying their peak position on the CCD. The fibre profile shape is then defined by fitting a Gaussian curve to the fibre flux in the Twilight flat frame. For each fibre of interest, the two surrounding fibres are fitted simultaneously to account for overlapping light from the surrounding profiles. This process is performed at various wavelength positions in order to map the fibre profile as a function of the spectrum direction. This is because the fibre shape can change with position on the CCD. Once the position and width profile of the fibres are defined, they are applied to all other observations.
5. Through applying the tramline map and fibre profile widths to all extracting frames, a 1D spectra for each fibre is extracted. This is achieved by calculating the total flux for all wavelength positions across all fibres.
6. Emission lines identified within the now extracted 1D spectra are compared to line lists for the CuAr arc frames. These features are used to wavelength calibrate the data, which are then resampled onto a wavelength grid that is consistent for all fibres.

The creation of RSS frames through individual fibre spectrum processing with 2dFDR is now complete.

2.4.2 Obtain science-ready data cubes from RSS files using PyKOALA

Once the RSS frames have been obtained, we passed them through custom Python scripts as well as the PyKOALA code (López-Sánchez et al. in prep) to produce the final, science-ready data cubes. PyKOALA routines allow us to mask defects, perform the throughput correction for all fibres, the sky subtraction, the absolute flux calibration, and the correction for atmospheric refraction, to properly align all the individual dithered frames, and mosaicking individual objects into a final data cube.

Throughput Correction

Each fibre has unique characteristics, in terms of both the total throughput of light and its dependence on wavelength. We need to correct for these characteristics to place each fibre on the same relative scale. Both of these effects are corrected for in a relative sense by using twilight flat observations. For the wavelength-dependent throughput correction, the mean twilight spectrum is determined by median combining the light from all fibres from the twilight RSS. Each fibre is then divided through by this mean spectrum, and the remaining spectrum gives the relative wavelength-dependent throughput for each fibre. Twilight flats are also used to determine the relative flux of each fibre by using the total flux measured from the twilight flat in the wavelength pixel range 100-1900. By comparing the relative flux to the mean distribution of fluxes for all fibres, the relative throughput is corrected. These corrections are applied to all observation frames.

Masking Defects

CCD defects and cosmic artefacts which were not identified by 2dFDR are also required to be corrected. These defects within the spectrum result in pixel wide peaks with intensities equivalent to the upper detection limit of the CCD, and significantly greater than the strongest emission feature. Therefore, these structures are identified through masking all pixels with a value similar to that of the upper CCD limit.

Sky Subtraction

As discussed in Chapter 3, our data is used to search for very faint emission lines which often lie close to regions affected by sky emission. Thus, accurate sky subtraction is very important within this work. Once the offset sky frames are throughput calibrated, there are two backgrounds which are required to be removed: the primary background and the residuals remaining from the initial sky-subtraction. The primary background subtraction is performed using a sky spectrum generated by the median combination of fibres with lowest 5% of the flux in the galaxy frames. This removes the majority of the sky background, however, on testing we identified a small residual background in the residuals of the sky-subtracted offset sky frames. A scaled version of the median combined and smoothed offset sky residual frames was subtracted from the galaxy frames to account for this small additional background.

Absolute flux calibration

To perform the absolute flux calibration of our data (i.e. the conversion between measured counts per pixel to physical units of flux) we use spectrophotometric standard stars. Once the data of these standard stars have been properly calibrated (throughput correction, wavelength calibration), sky-subtracted and corrected for extinction, we extract the integrated spectrum of the star using the data cube re-binned with the same parameters that we will use for obtaining our science 3D cubes. The extracted spectrum of the calibration star is then scaled to its known, absolute flux-calibrated, spectrum to get the conversion curve between counts per pixel and flux in units of $\text{erg cm}^{-2} \text{\AA}^{-1}$.

Telluric Correction

Telluric absorptions due to O_2 and H_2O in our atmosphere affects the spectra obtained with the red arm of AAOmega. These telluric features may affect the spectral measurements performed in Chapter 3, and thus require removal. For this we also use observations of spectrophotometric standard stars. The spectrum of a standard star is relatively smoothly varying around the regions of the telluric absorption lines which were identified as ranges 6450–6700 \AA , 6850–7050 \AA , and 7130–7380 \AA . The continuum surrounding the telluric absorption is modelled by a smoothly varying polynomial function, which is subsequently divided out of the data leaving a purely telluric spectrum. All galaxy spectra are then divided by this telluric spectrum.

Cartesian Grid Data Cubes Creation

Once the fully calibrated RSS is obtained it is required to generate Cartesian grid data cubes to be able to spatially analyse features within these galaxies. The cube creation pipeline for the KOALA data is a fundamental task of the PyKOALA scripts. It follows a very similar procedures to that described by Sharp et al. (2015) for SAMI IFU data.

The RSS files are re-binned onto a Cartesian grid in the form of a cube. A small spatial offset was applied to each observed galaxy frame to produce a series of dithered observations for cube reconstruction. The re-binning, realigning and stacking all dithered object frames will allow outlier rejections, increased signal-to-noise (S/N) ratio for all fibres, correction of dead fibres, and easier visualisation of resulting data products. These processes are described below.

To obtain a more visual representation of the FoV, all fibre spectrum are re-positioned to form a cube structure as seen in Figure 2.1. RSS frames display wavelength against fibres in 2D images,

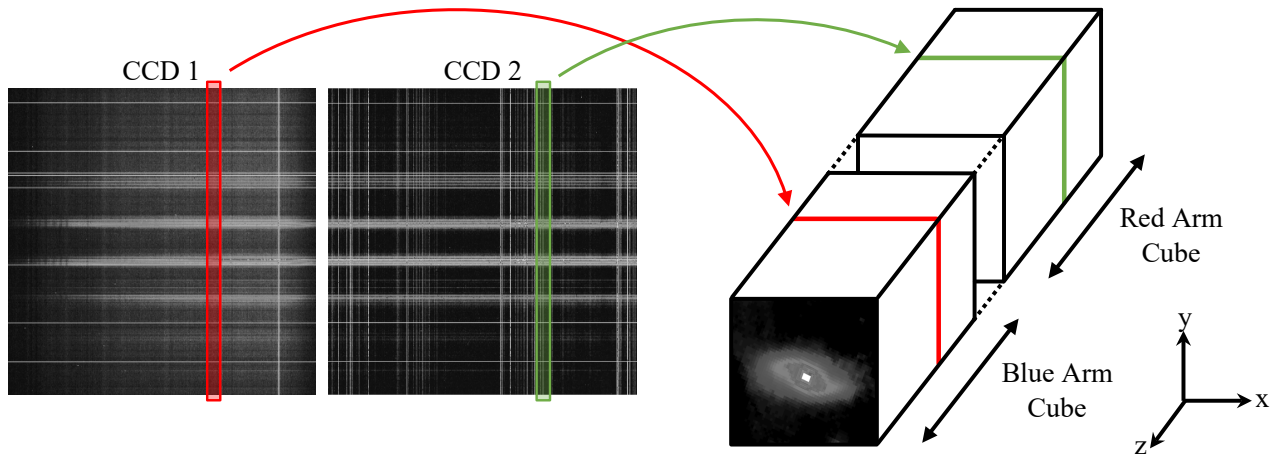


FIGURE 2.1: This figure reveals the transition of fibres from RSS into a data cube. The left hand side object represents the RSS, where the x-y plane represents the wavelength against fibre number. Each wavelength slice within the RSS is mapped onto a corresponding slice within the right hand side object. This structure symbolises the three dimensional structure of the data cube created. The x-y plane represents a slice across a specific wavelength in the z plane for all spectra. Each slice is created through re-positioning the pixels within the reduced data results.

making it challenging to easily identify the location of the fibre within the FoV. Therefore, data cubes are created, where the x , y and z axes represent the Right Ascension (R.A.), the Declination (dec.) and the wavelength (in Angstroms, \AA) of the field, respectively. Since each pixel within the created data cube contains a spectrum, they are hereafter referred to as spaxels. Each spaxel within a wavelength slice of the cube is comparable to the fibre position taken with KOALA+AAOmega. Thus, re-sampling each fibre within the RSS frame to its known equivalent position on a Cartesian grid will produce the required cube structure. Figure 2.1 displays this, as each wavelength slice for the blue and red arm CCD, shown by the coloured regions on the RSS frames to the left, is mapped to its corresponding slice within the data cube, indicated by the same colour slice within the cube displayed on the right. In its wide-field mode, the KOALA instrument lenslets are 1.25 arcsec in size. This is comparable to the median seeing at the AAT (1.6 arcsec). Therefore, in this instrument setup the point-spread function (PSF) is undersampled. The processes of dithering and resampling onto a cube corrects for this. To account for this, each frame is mapped onto a Cartesian grid with 0.6 arcsec spaxels. Each wavelength slice within the cube displays all fibres on a Cartesian grid, thus allowing the investigation of specific emission features.

The effects of differential atmospheric refraction shift the galaxy centroids as a function of wavelength, and must be corrected prior to combining the frames. To do this, the centroid of each galaxy is identified as a function of wavelength, and then shifted to a common position. Therefore, through redefining the central pixel the location of the galaxy upon the frame is determined with high accuracy.

In order to significantly increase S/N, as well as account for unusable CCD pixels, and to widen the FoV, all dithered object frames are median stacked to produce a single data cube. The central intensity peaks identified when performing differential atmospheric refraction corrections, are aligned within the same Cartesian grid and stacked together for the blue and red arm separately. Data cubes for both the blue and red arms are further aligned onto a new Cartesian grid, and produced for each galaxy. These cubes are fully reduced and able to be analysed within the following chapters.

Observation Date		2016 Oct 24 th			2016 Oct 25 th		
Observation Types	Runs	Exposure Time [s]	Seeing [arcsec]	Runs	Exposure Time [s]	Seeing [arcsec]	
Dark	10	1800	1.3 - 2.0	8	1800	1.4 - 2.0	
Arc (CuAr)	1	2	1.3 - 2.0	2	2	1.4 - 2.0	
Detector Flats	2	10	0.8	2	10	1.1	
Twilight Sky Flat	4	60 - 240	1.3 - 2.0	4	20 - 60	1.1	
9011900084 Object	7	1800	1.2 - 2.2				
9011900084 Offset Sky	4	600	1.2 - 2.2				
9011900166 Object				10	1800	1.1	
9011900166 Offset Sky				5	600	1.1	
Standard Stars	3	180	1.3	3	180	1.4 - 2.0	
Bias	20	0	1.3				

TABLE 2.2: Observation Log for KOALA for each CCD

Observation Types	Runs	Exposure Time [s]	Seeing [arcsec]
Dark	18	1800	-
Detector Flats	47	120	-

TABLE 2.3: Observation Log from other nights, obtained from the AAT archive, for each CCD

Results and Analysis

The primary aim of this thesis is to test the RPS-induced quenching hypothesis for these galaxies put forward by Owers et al. (2019). Structures of ionised emission reveal features such as tails of stripped gas, providing direct evidence for the RPS effects upon a galaxy that can also be used to infer direction of motion in the plane of the sky (Smith et al., 2010; Boselli et al., 2018b). In order to detect these faint features, emission lines must be accurately measured as described in the following sections. This enables the investigation into the origin of ionised gas, the morphology of gas outflows.

3.1 Line Strength Measurements

In this section we describe the procedure for defining the stellar continuum and for measuring emission and absorption line fluxes.

3.1.1 Voronoi Binned Data

Adaptive binning is used to preserve spatial resolution in regions where the spectra already contains high S/N but combines regions which do not have adequate S/N for continuum definition into bin regions. Utilising Voronoi binning techniques laid out by Cappellari (2009), spaxels with S/N below the minimal limit specified are binned using a Voronoi tessellation into nearly hexagonal lattices containing neighbouring spaxels. When accumulated, each newly formed section will achieve the desired S/N limit.

The variance was not propagated through the data reduction process laid out previously. We therefore estimate the noise in each spaxel empirically from the spectra. The noise is estimated by taking the Median Absolute Deviation (MAD) within a $\pm 100 \text{ \AA}$ window around observed wavelength 4100 \AA ($4000\text{--}4200 \text{ \AA}$). The median signal value within this same window was also produced. Taking

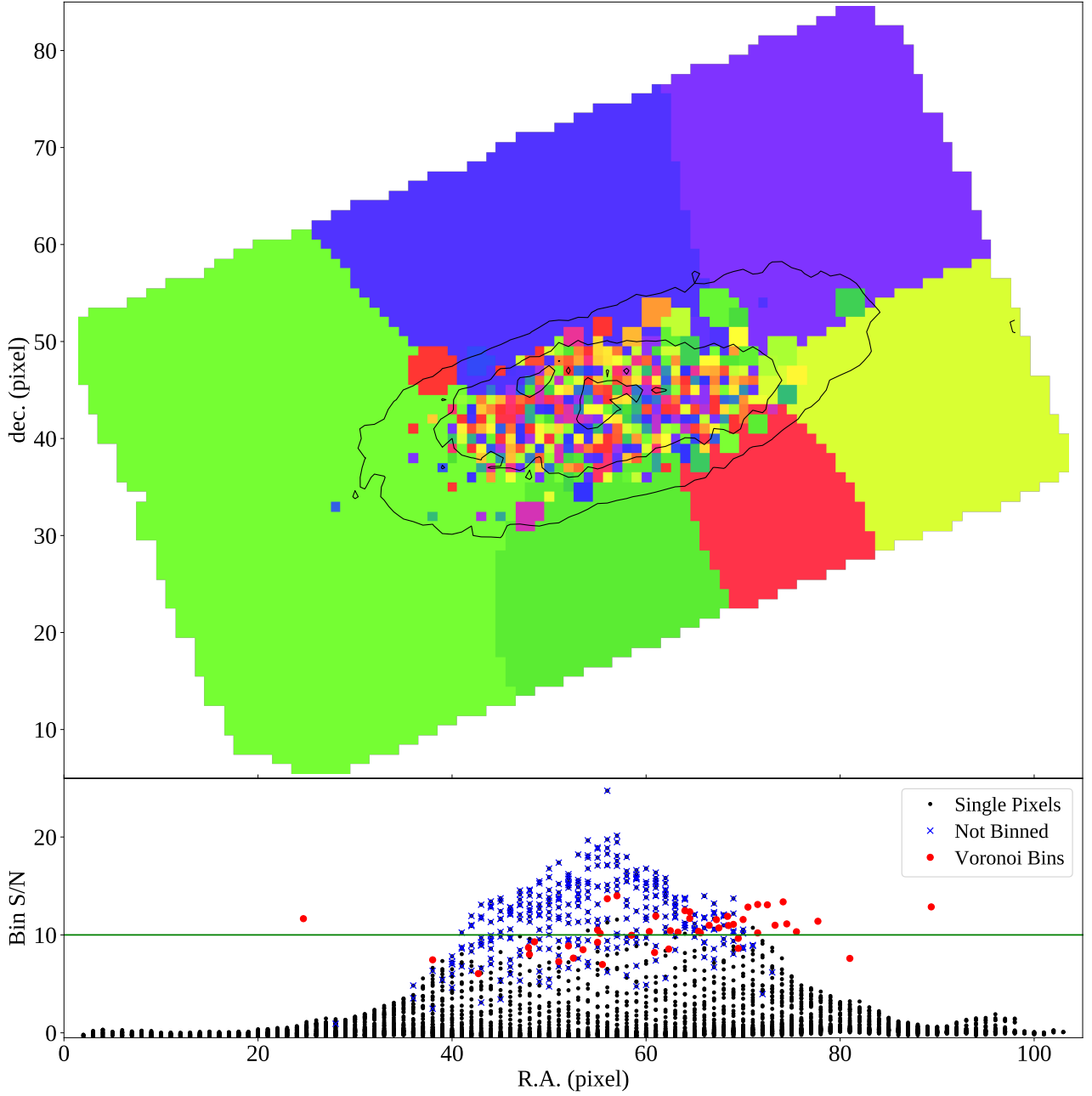


FIGURE 3.1: Voronoi binning output of the blue arm for galaxy 9011900084 for the blue arm. *Top panel:* The regions selected to be combined in order to achieve the input S/N limit are shown through the various coloured segments with an overlaid contour representing the outskirts of the stellar disk. *Bottom panel:* This reveals the S/N scatter in Voronoi binning of these galaxies. The original S/N of the pixels is shown with the black points, while the red circles and blue crosses indicate the combined S/N of Voronoi binned regions. The red circles symbolise bins covering more than a single pixel, where the blue crosses symbolise Voronoi bins which only contain a single pixel. The target S/N=10 is indicated by the green horizontal line.

the ratio of these signal and noise values for all spaxels will produce a single 2D map to which the Voronoi tessellation can be applied. The minimum S/N value of 10 was selected, such that any spaxel containing $S/N > 10$ are not binned and generally reside towards the central regions of the galaxy as demonstrated by the maps of Voronoi bins in Figures 3.1 and 3.2.

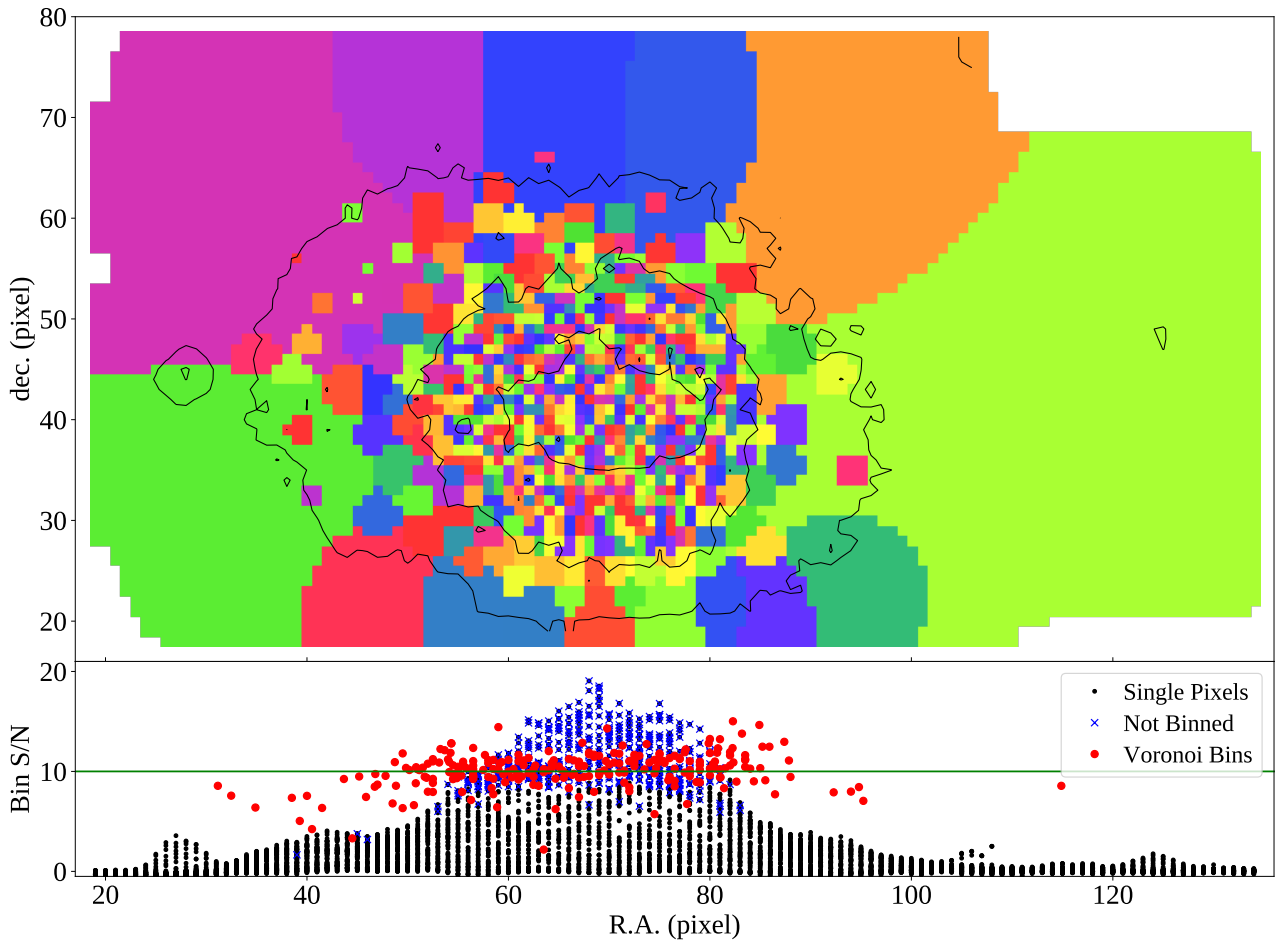


FIGURE 3.2: Same as Figure 3.1, but for galaxy 9011900166

For consistency of bin positions between the blue and red arms, this binning process was performed on the blue arm of the KOALA data first and these bins are then applied to the red arm. This process was also performed due to the majority of prominent absorption features, useful for characterising the underlying stellar population which is required for good continuum subtraction, being found in the blue arm.

3.1.2 Continuum definition for individual spaxels

Emission lines lie on top of a stellar continuum that contains absorption features. In particular, Hydrogen Balmer emission lines lie directly on top of their absorption-line counterparts. This can significantly affect emission line flux measurements. Therefore, accurate modelling of the stellar continuum is required in order to measure accurate emission line fluxes. The stellar continuum is fit on a spaxel-by-spaxel basis using the penalised pixel-fitting routine (pPXF, Cappellari & Emsellem 2004; Cappellari 2017). pPXF extracts galaxy stellar kinematics (v_{stellar} , σ_{stellar} , $h3$, $h4$, ...), stellar

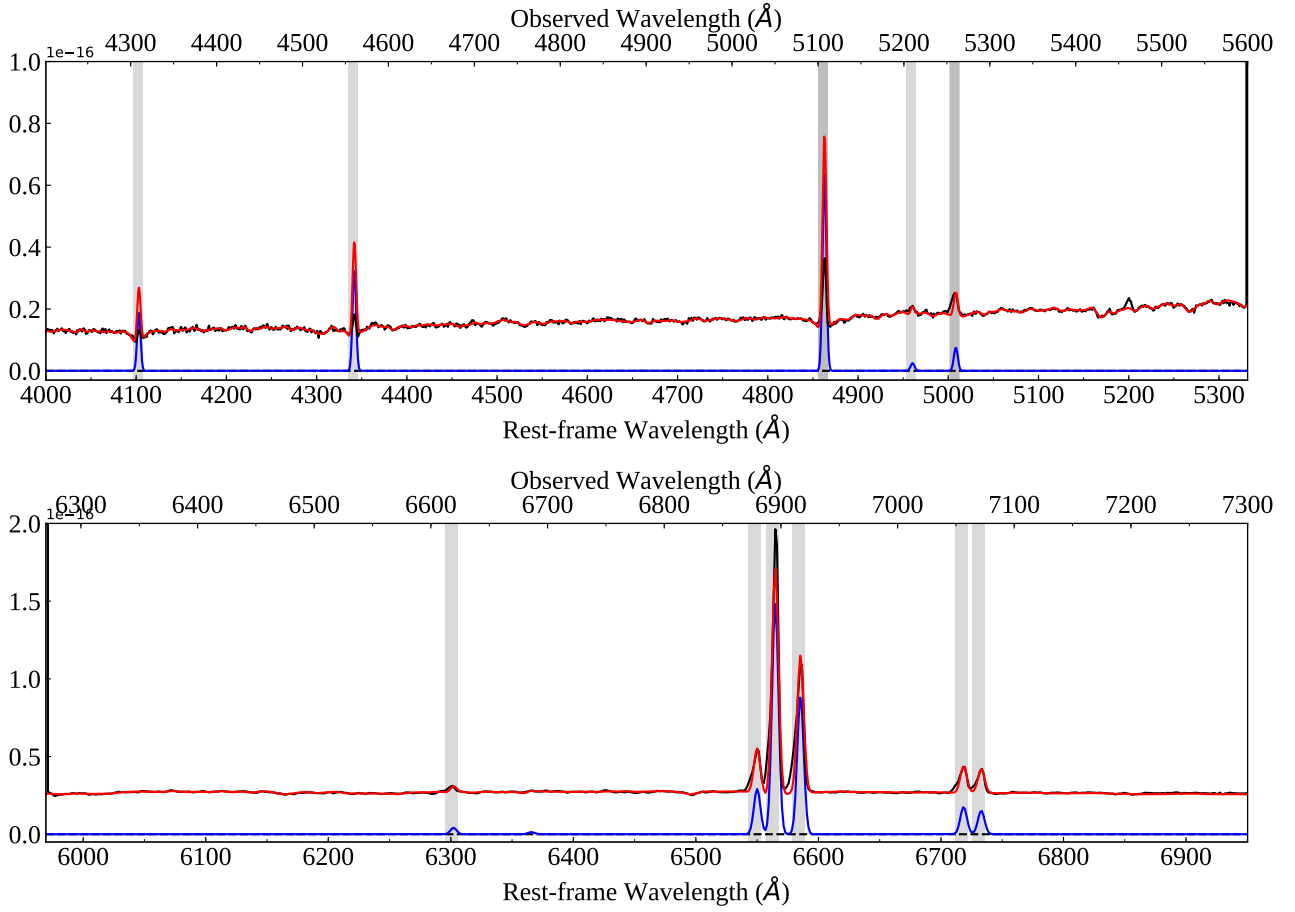


FIGURE 3.3: Spectra from the central spaxel within the galaxy 9011900084 containing the highest S/N value. This figure shows the stellar continuum fitting process of galaxy 9011900084 for the blue and red arms (upper and lower panels respectively). The black line indicates the input spectrum. The shaded regions indicate the wavelength ranges excluded during the kinematic fitting component of the process. The masks are then lifted, and the emission lines are fitted. The blue curve represents the pPXF gas best fit. The wavelength ranges shown correlate with the wavelengths selected to be fit, being 4200–5600 Å (upper panel) and 6270–7300 Å (lower panel) for observed wavelengths. This selection resulted in the removal of extremely poor fits at the blue and red extremes of the blue and red arm spectra.

population, and gas emission line fluxes through fitting Stellar Population Synthesis (SPS) templates, drawn from the MILES (Vazdekis et al., 2010) libraries, to each individual spectrum in pixel space. Through this process, more accurate emission line values are measurable, allowing the creation of emission line ratios (such as $[\text{N II}]/\text{H}_\alpha$) which aid in the identification of features as either due to: star formation, shocked ionised gas, or an active galactic nucleus (AGN, e.g. Ho et al. 2014). Within this work, the multi-step procedure followed is similar to that outlined within the previous investigation of these galaxies by Owers et al. (2019).

The first step was to combine the blue and red data cubes to create a single data cube, as seen in Figure 2.1. Before the combination, observed wavelength ranges were selected as 4200–5600 Å and 6270–7300 Å for the blue and red arms respectively and the high resolution red arm spectra

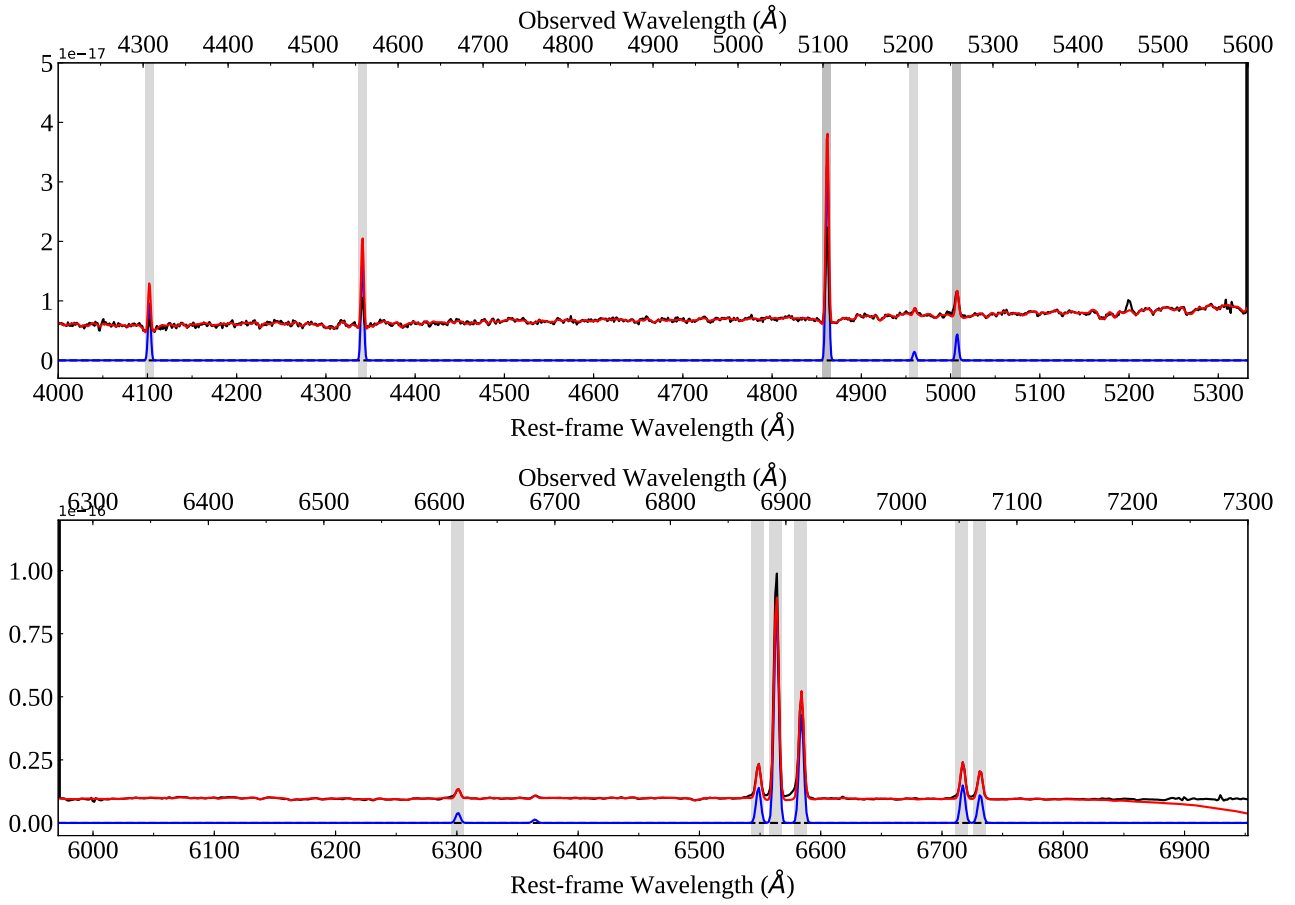


FIGURE 3.4: Same as Figure 3.3, but for galaxy 9011900166

was convolved to match the resolution of the blue arm as well as resampled onto the blue arm wavelength solution. Wavelength regions at the blue and red ends of the spectra are excluded because they are affected by artefacts that remained following data reduction. As the templates used contain wavelengths as measured at a rest frame, in order to accurately compare these with the observed spectra the observed wavelength is thus converted into the rest frame. This is achieved through using $\lambda_{\text{rest}} = \lambda_{\text{observed}} / (1 + z)$, where z is the redshift of the galaxy investigated as stated within Table 2.1 (Owers et al., 2017).

In order to fit the kinematics and emission features within the spectra, the combined spectra from the Voronoi binned regions are run individually through the pPXF process. pPXF is initially performed to obtain stellar kinematic components. Thus, emission lines are masked, as shown in Figures 3.3 and 3.4, and an additive polynomial is used to remove residuals from small errors in the flux calibration (van de Sande et al., 2017). The kinematic v_{stellar} and σ_{stellar} parameters are initially assumed to be 0 and 150 within the set boundaries $[-500, 500]$ and $[0.1, 400]$ respectively for both kinematics and gas components of the galaxy. Unregularised fits (REGUL=0) for spectral regions are also run, which are

excluding emission line and bad pixel (no value) regions. The resulting best fit model outputted from pPXF is subtracted from the spectrum to produce a residual spectrum for each spaxel. This residual spectrum is used to determine a more accurate noise spectrum. A second kinematics pPXF is run in order to implement the corrected noise value and initial stellar kinematic parameters, thus obtaining a more accurate kinematics spectral fit and stellar kinematic values.

Once the final kinematics pPXF fit is produced, outputted kinematics are used as the initial estimation to perform the emission line pPXF calculations. For this to occur, the kinematics are fixed and multiplicative polynomials are used for fitting to account for template mismatch due to possible bad SPS templates and imperfect flux calibration, as well as dust reddening. The output result represents the best fit for each spaxel, produced through the weighted combination of inputted templates. These outputs are revealed within Figures 3.3 and 3.4, which show the original spectrum (black line), overlaid with the best fit (red line) and gas best fit (blue line) data. The figures reveal the spectra for the central spaxel position within the data cube containing the highest S/N value which exceeds the Voronoi bin limit. This spaxel is therefore its own Voronoi Bin.

Especially in the outskirts of the galaxy FoV, Voronoi bins contain multiple spaxels which were combined to produce a single spectrum during the initial pPXF analysis. This provided corrections to the initial v_{stellar} and σ_{stellar} estimations as well as created a list of templates which best reproduce the combined spectra within the selected Voronoi Bin regions. This limited set of templates is then used as input to pPXF when fitting each individual spaxel within the selected Voronoi bin, while the kinematics from the binned fit are used as initial inputs. In cases where the S/N is too low in the single spaxel, the kinematics are fixed at the Voronoi bin values, while the single best-fit template from the Voronoi bin is used. However, if the number of dead pixels (defined as spectrum pixels which have either no finite value or contain zero intensity) exceed 10% of the overall pixels within the investigated wavelength ranges then those spaxels are excluded from being fit. This is important in the outer parts of the galaxies, where continuum fluxes are low.

The same process was performed for individual spaxels as laid out for the Voronoi bin combined regions. Through constraining the continuum fit initially to the Voronoi bin regions, more reliable results from the emission line fluxes at low continuum S/N values are obtained. This was significant towards the outer environmental regions of the galaxy which contain minimal features.

Emission Line	Rest-frame Wavelength [\AA]
H_δ	4101.76
H_γ	4340.47
H_β	4861.33
[O III]	4958.92, 5006.84
[O I]	6300.30
H_α	6562.82
[N II]	6548.03, 6583.41
[S II]	6716.47, 6730.85

TABLE 3.1: Emission lines considered in this study. The columns of the table are emission line names on the left and their corresponding wavelength at rest-frame on the right. The emission doublet [S II] is hereafter referring to the combination of flux produced from both wavelengths listed.

3.1.3 Emission line flux measurements

Flux, flux error, and flux Amplitude over Noise (AoN) are measured for the emission lines with wavelengths listed in Table 3.1, as highlighted by grey regions within Figure 3.3 and 3.4, along with Velocity (V) and Velocity Dispersion (σ) of both the stellar and gas fit components outputted from pPXF. These results are obtained for all spaxels within the data cube to produce maps for each line species.

Flux values are obtained through the use of $F = \sqrt{2\pi} A \sigma_{\text{tot}}$, where A is the line amplitude measured through determining the maximum value within a $\pm 5 \text{ \AA}$ window around the emission line in order to account for slight wavelength shifts and neighbouring emission features. σ_{tot} is the total dispersion of the line as defined in Equation 3.1 below:

$$\sigma_{\text{tot}}^2 = \left(\sigma_{\text{ins}} \frac{1}{1+z} \right)^2 + \left(\frac{\lambda_{\text{line}} \sigma_{\text{gas}}}{c} \right)^2 \quad (3.1)$$

This contains the KOALA+AAOmega instrument resolution (σ_{ins}), redshift of the galaxy (z), the wavelength of the calculated emission line (λ_{line}), gas velocity dispersion calculated by pPXF (σ_{gas}), and the speed of light (c).

As a variance array was not produced from the data reduction, it is required to quantify the errors associated with the measurement of flux. This is essential in order to distinguish reliably measured, high S/N line fluxes from where the model has fitted noise spikes. The empirically based method

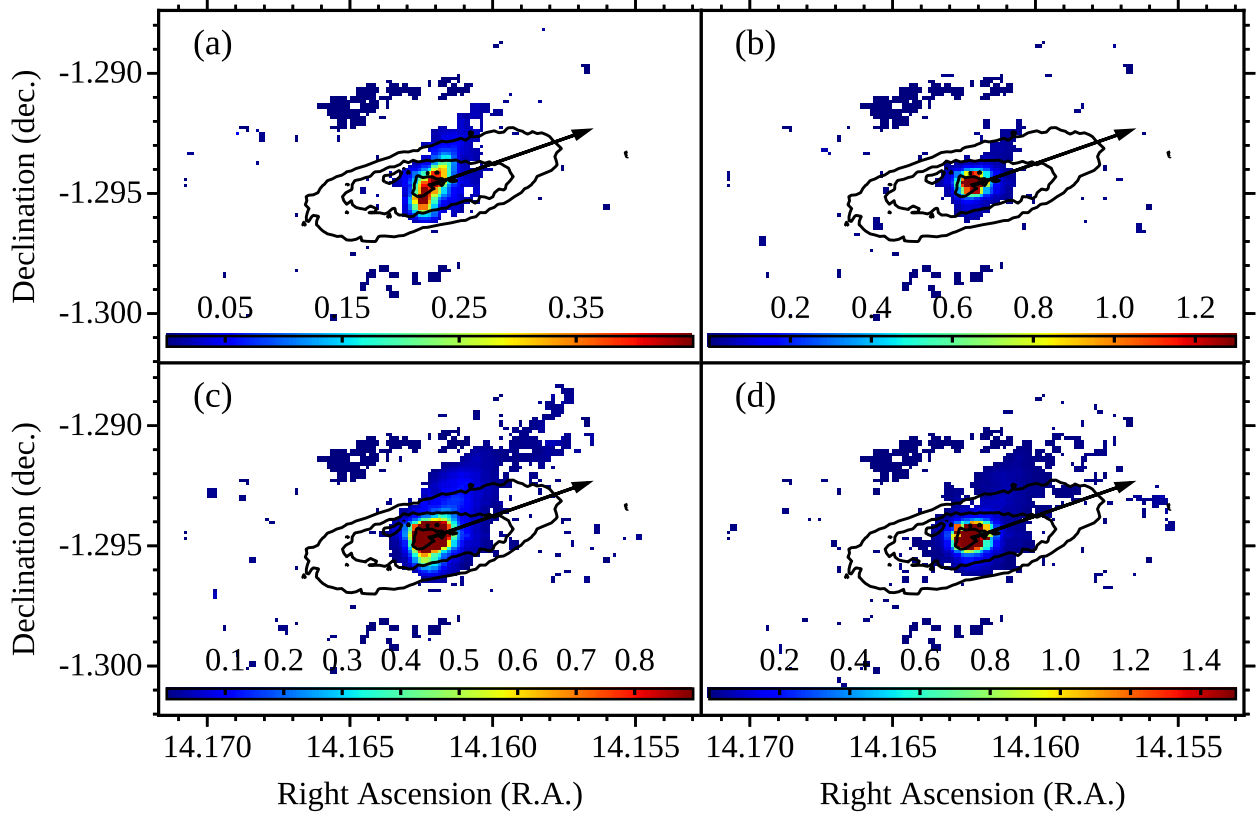


FIGURE 3.5: 9011900084: Flux maps for [O III] (top left), [S II] (top right), [N II] (bottom left), and H_α (bottom right) with colourbar units as $10^{-16} \text{ erg cm}^{-2} \text{ s}^{-1}$ per $0.6''$ pixel. The contours represent the outskirts of the stellar disk within all panels. North is towards the top of the page and West is towards the right.

described by Lenz & Ayres (1992) to determine the S/N ratio of the flux used the following:

$$(S/N)_x = 0.67 \left(\frac{\text{FWHM}}{\Delta\lambda} \right)^{1/2} (S/N)_0, \quad (3.2)$$

where $\text{FWHM} = 2.355 \sigma_{\text{tot}}$ is the Full Width at Half Maximum of the Gaussian profile, and $\Delta\lambda$ is the pixel size in Angstroms (\AA). The S/N ($(S/N)_0$) value is obtained through the ratio of the Amplitude (A) of the emission line Gaussian profile, as defined above, to the Median Absolute Deviation (MAD) of the residuals within the $\pm 50 \text{ \AA}$ window around the emission line. Figures 3.5 and 3.6 therefore show [O III], [S II], [N II], and H_α emission line maps containing only spaxels with $S/N > 3$, where S/N now represents Amplitude/Noise.

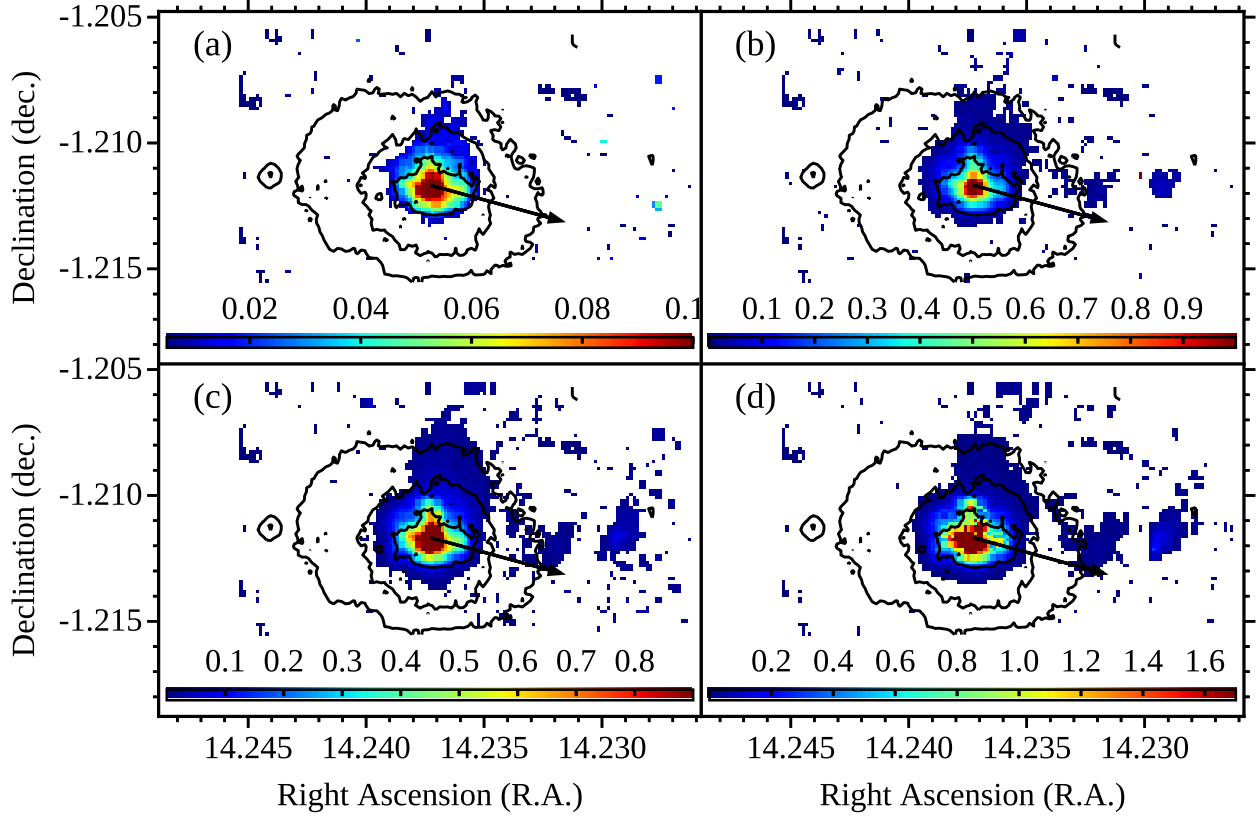


FIGURE 3.6: 9011900166: Flux maps for [O III] (top left), [S II] (top right), [N II] (bottom left), and H_α (bottom right) with colourbar units as $10^{-16} \text{ erg cm}^{-2} \text{ s}^{-1}$ per $0.6''$ pixel. The contours represent the outskirts of the stellar disk within all panels. North is towards the top of the page and West is towards the right.

3.2 Results

3.2.1 Ionised gas properties of 9011900084 and 9011900166

One-sided tails of ionised emission have previously been investigated within surveys such as VESTIGE (Boselli et al., 2018a), MUSE (Fumagalli et al., 2014), ACCESS (Haines et al., 2011), and GASP (Poggianti et al., 2017c), typically revealing the presence of jellyfish galaxies. These emission features are interpreted as very strong evidence for ICM-ISM-related processes, such as ram-pressure stripping. Having obtained the resolved emission line flux maps, we can now search for such features for the galaxies 9011900084 and 9011900166.

Figures 3.5 and 3.6 for galaxies 9011900084 and 9011900166 respectively show [O III], [S II], [N II], and H_α emission line flux maps containing spaxels with $S/N > 3$. Contours within these maps represent the galaxy limits of the stellar components of the galaxies, as defined to be an $S/N = 1.5$ limit of the stellar continuum within a 100 \AA window around 4100 \AA . Clear evidence of one-sided emission which extends off the contoured plane of the galaxy is observed. The length of the tails and how far

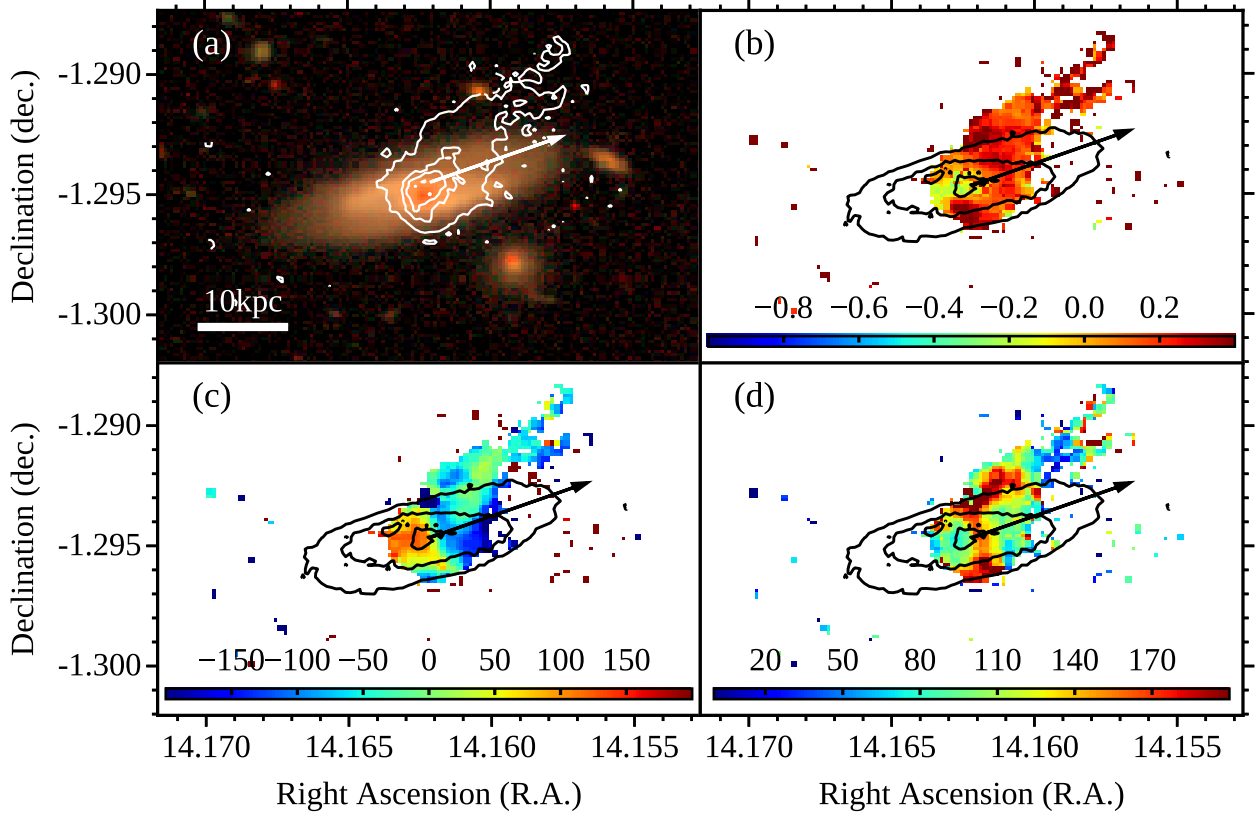


FIGURE 3.7: 9011900084: SDSS Image (top left), $[\text{N II}]/\text{H}\alpha$ Flux Map (top right), Velocity V_{gas} (bottom left), and Velocity Dispersion σ_{gas} (bottom right). The contours reveal $[\text{N II}]$ flux map lines at $\text{S/N}=[3, 25, 55]$ within the top left panel, indicating the presence of gas tails, and the remaining panels contain contours representing the outskirts of the stellar disk. North is towards the top of the page and West is towards the right.

off the plane of the galaxy's stellar disk they extend is able to be quantified through the use of $[\text{N II}]$ emission features. In both galaxies 9011900084 and 9011900166, one-sided extraplanar ionised gas is observed to extend respectively ~ 25.2 kpc and ~ 18.4 kpc from the centre of the galaxy, and ~ 16.1 kpc and ~ 6.1 kpc from the outskirts of the stellar disk. This reveals that galaxy 9011900166 has a tail less than half that of 9011900084 projecting from its disk.

Upon comparing these emission features it is seen that $[\text{O III}]$ and $[\text{S II}]$ contain the weakest flux, where a $[\text{N II}]$ and $\text{H}\alpha$ reveal a significantly greater fluxes, which extend farther beyond the stellar component of both galaxies when compared with the $[\text{O III}]$ and $[\text{S II}]$ emission. The $[\text{N II}]$ flux is stronger than that of the other lines in the outer parts of the galaxies, and the surface brightness limit for these tail features along the $[\text{N II}]$ $\text{S/N}=3$ contour is $\sim 2 \times 10^{-18} \text{ erg s}^{-1} \text{ cm}^{-2} \text{ arcsec}^{-2}$ per $0.6''$ pixel. Therefore, the flux distribution of this line is used to define the boundaries of the tails below.

The direction of motion of galaxies may be determined through the investigation into tail features. These arise as gas is removed from galaxies as they travel through the ICM. Ratios of emission features

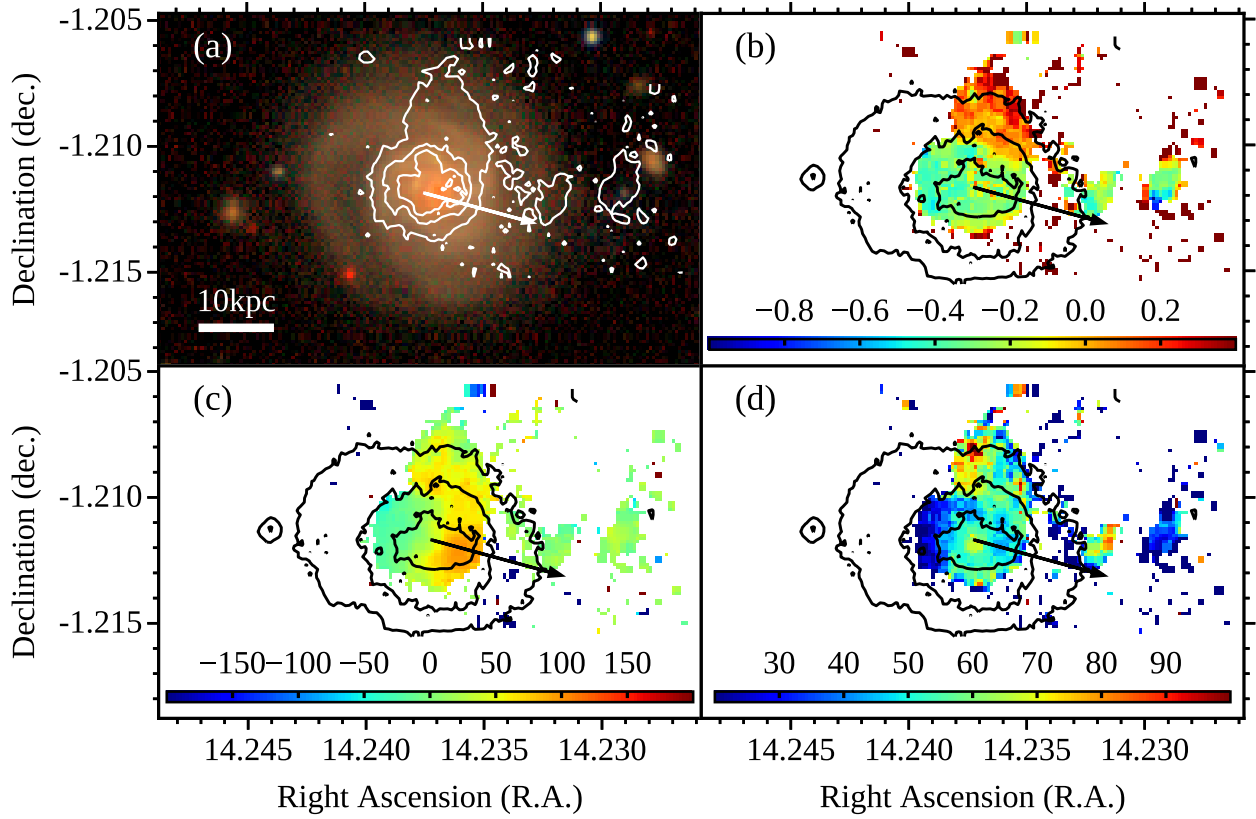


FIGURE 3.8: 9011900166: SDSS Image (top left), $[N II]/H_\alpha$ Flux Map (top right), Velocity V_{gas} (bottom left), and Velocity Dispersion σ_{gas} (bottom right). The contours reveal $[N II]$ flux map lines at $S/N=[3, 25, 55]$ within the top left panel, indicating the presence of gas tails, and the remaining panels contain contours representing the outskirts of the stellar disk. North is towards the top of the page and West is towards the right.

are typically used to investigate the ionisation properties of the gas. This is initially shown in Figure 3.7 and 3.8 for galaxies 9011900084 and 9011900166 respectively. Panel (a) contains an SDSS image of the galaxies overlapped with the $[N II]/H_\alpha$ contour around $S/N=3$. Panels (b) reveal the 2D map of the $\log([N II]/H_\alpha)$ ratio, computed for all spaxels in which their $S/N>3$. This ratio reveals the ionisation mechanism as being either due to star-formation ($\log([N II]/H_\alpha) < -0.32$); a shock front, LINERs, or AGNs ionising the gas within this region ($\log([N II]/H_\alpha) > 0.1$); or a combination of both to produce composite regions ($-0.32 < \log([N II]/H_\alpha) < 0.1$) as laid out previously by Cid Fernandes et al. (2010). For 9011900084, the majority of the galaxy and all tail features are not SF, and the ionisation is potentially due to shock produced by RPS. The central region of the galaxy however is defined within the composite level between SF and non-SF. Galaxy 9011900166 shows strong SF within the central region of the galaxy, and non-SF ionised gas within the tail.

Panels (c) and (d) show the pPXF kinematics results of V_{gas} and σ_{gas} respectively. Gas within

9011900084 rotates about the N-S axis with maximum absolute line-of-sight velocities of order 100–130 km/s. Their gas tails show an overall motion retreating from the line of sight with a non-smooth distribution. The gas tails are observed to approach higher velocities than their corresponding disk counterparts. Similarly, 9011900166 rotates about the N-S axis with maximum absolute line-of-sight velocities of order 15–100 km/s, with gas tails observing higher velocities than their corresponding disk counterparts.

Within each panel of these figures, the arrow from the centre of the galaxy identifies the direction of the galaxy cluster centre. The furthest extension point of the tail in relation to the centre of the galaxy may reveal the galaxies overall direction of motion. For galaxy 9011900084, the direction of the galaxy tail is pointing from the centre of the galaxy towards a North-West direction in the plane of the sky. The centre of the cluster is located to the right of the tail, however, still in the general North-West direction. This means that the projection of the galaxy tail has less than 90° separation from the direction to the cluster centre. Galaxy 9011900166's tail extends from the centre of the galaxy in a North-North-West direction in the plane of the sky. The centre of the cluster is located approximately 90° to the right of the tail, extending towards a southerly direction. Through these comparisons, a conclusion may be drawn regarding the overall direction of motion of the galaxy.

3.2.2 Detailed Analysis of Individual Regions

In Section 3.2.1, we found that the ionised gas in the tails showed several distinct features when compared with that found in the galaxies. However, the weaker line species, such as [O III] and [S II], are too weak to be detected in the single-spaxel data. The stacking of spectra from regions of interest enable a more detailed line ratio analysis to be performed due to previously weaker lines becoming more prominent with a greater S/N value.

As seen in Figures 3.9 and 3.10 for galaxies 9011900084 and 9011900166 respectively, within the contour regions confined by the [N II] flux region with $S/N > 3$ (blue contour), 5 regions were selected based on their position with respect to the stellar component of the galaxy (black outlined regions), and the value of the $\log([N II]/H_\alpha)$ ratio as displayed. The 'Front' was selected based on its higher [N II]/ H_α ratio values than surrounding regions, which indicates that violent interaction are occurring within this region. This, along with the tail on the opposite side of the galaxy disk, implies that this region may be the front region at the interface of the ICM and ISM. The 'Centre' was selected to represent the central area of the galaxy which contains a lower [N II]/ H_α ratio, hinting that the gas within this region is being ionised by ongoing star formation. The 'Outer Tail' represents the region

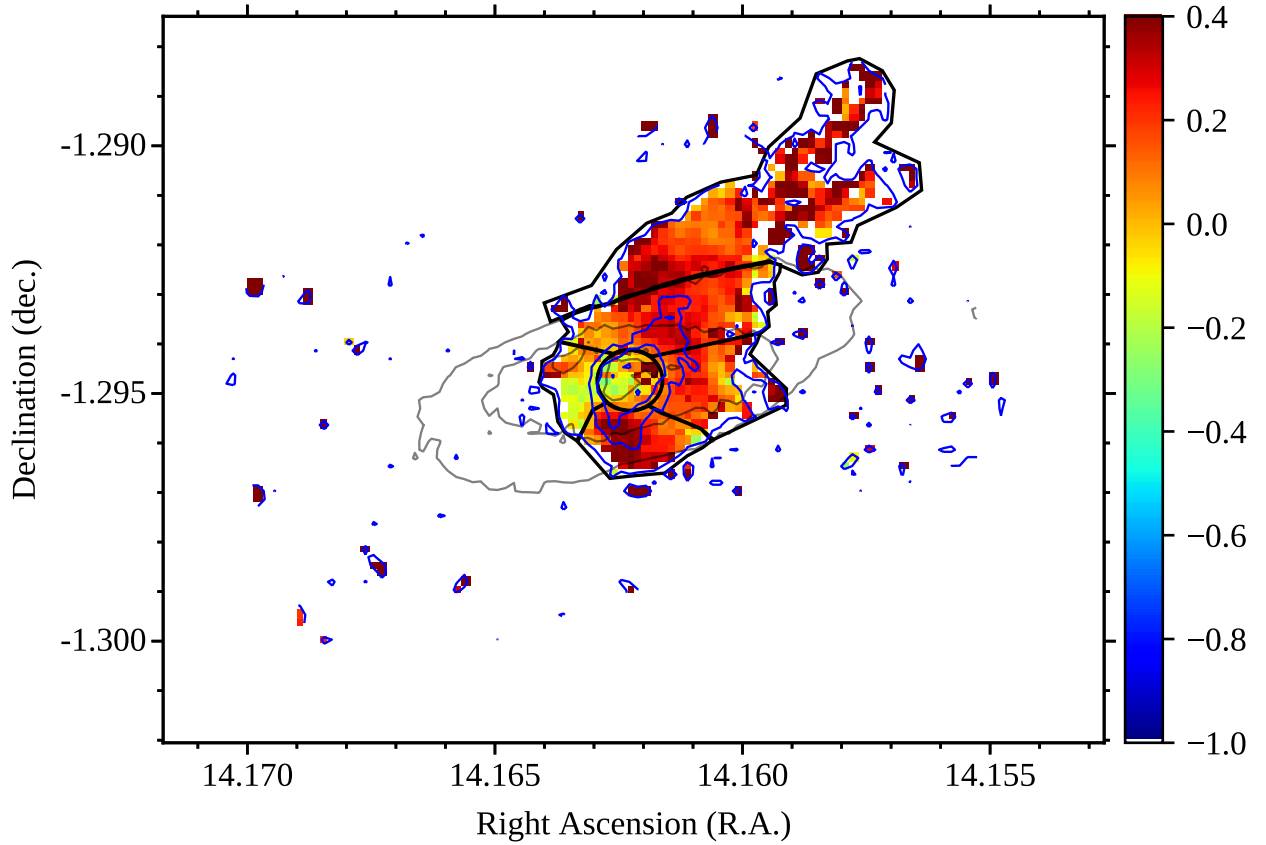


FIGURE 3.9: 9011900084: This figure displays the flux ratio map $\log([\text{N II}]/\text{H}_\alpha)$ which assists with the identification of the gas ionisation mechanism. Overlaid contours represent the outskirts of the stellar disk (grey), and $[\text{N II}]$ flux intensity for $\text{S/N} > 3$ region indicating the presence of gas (blue). Black apertures represent selected regions used to create the high S/N composite spectra. North is towards the top of the page and West is towards the right.

outside the galaxy which is displayed by the contour region. The ‘Inner Tail’ resides between the ‘Outer Tail’ and the ‘Centre’ in order to investigate the gas as it is in the process of leaving the galaxy to become the ‘Outer Tail’. Remaining regions within the stellar disk are lastly defined as the ‘Sides’.

All spaxel spectra within each region is therefore combined and run through pPXF as laid out within Sections 3.1.2 and 3.1.3. A list of the fluxes, uncertainties and the kinematical components (V_{gas} , σ_{gas}) for the different regions are displayed within Tables 3.2 and 3.3 for galaxies 9011900084 and 9011900166 respectively. The stacked $[\text{N II}]$ flux measurement for the outer tail emission feature of both galaxies approximate $\sim 10^{-15} \text{ erg cm}^{-2} \text{ s}^{-1}$, with a S/N averaging 10. Stacked spectra within the regions specified previously provides a higher S/N and stronger emission features which thus enable a more reliable measure of the line ratios.

Baldwin, Phillips & Terlevich (1981) were one of the first to investigate line ratio diagrams, more commonly referred to as BPT diagrams, in particular $[\text{N II}]/\text{H}_\alpha$ vs $[\text{O III}]/\text{H}_\beta$. Intensity ratios of pairs

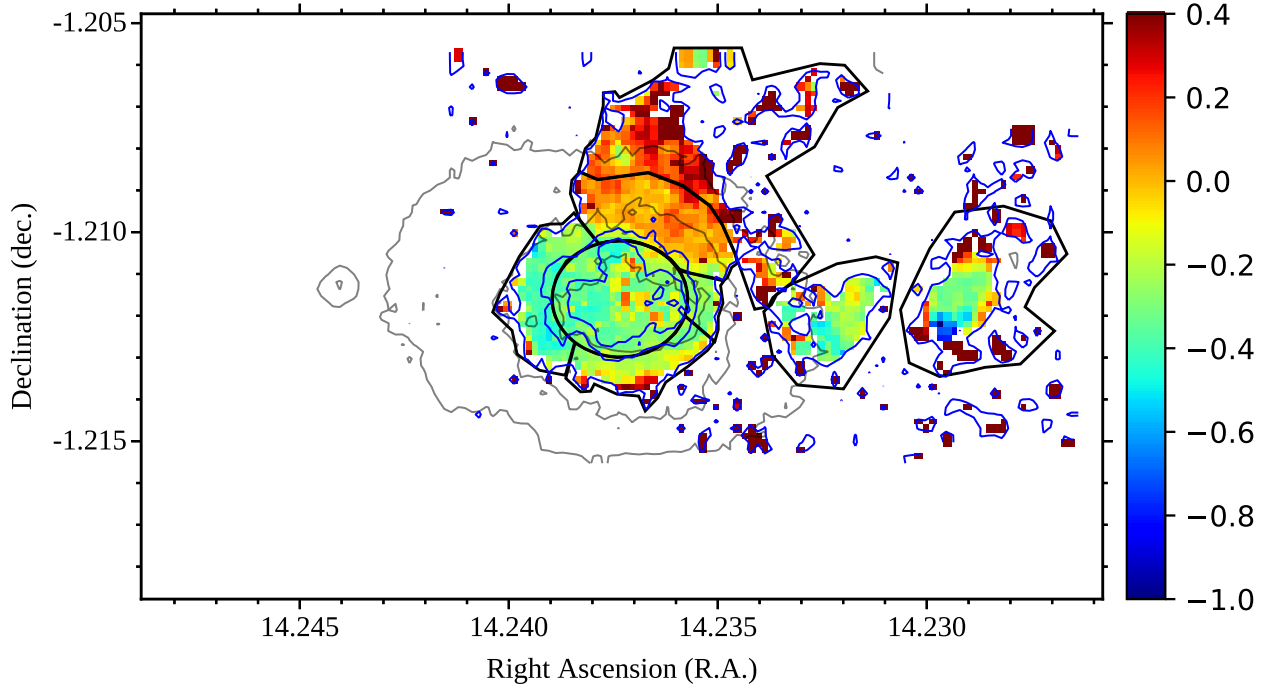


FIGURE 3.10: Same as Figure 3.9, but for galaxy 9011900166. North is towards the top of the page and West is towards the right.

of strong emission lines allows us to measure various aspects of the excitation level in each object, thus creating a graphical approach to classify objects. The work by Kewley et al. (2006) utilises BPT diagrams in order to highlight the open questions surrounding the ability to classify galaxies such as SF galaxies, Seyferts, and low-ionisation emission-line regions (LINERs) and how their differences may be used to identify them.

Kewley & Dopita (2002) provides a theoretical basis for the distribution of AGN and SF galaxies on the BPT diagram, providing a ‘maximal starburst’ line and clear divisions between non-SF and SF ionising sourced galaxies. These regions are separated through the following equations:

$$\log([\text{O III}]/\text{H}_\beta) = 0.61/(\log([\text{N II}]/\text{H}_\alpha) - 0.47) + 1.19 \quad (3.3)$$

$$\log([\text{O III}]/\text{H}_\beta) = 0.72/(\log([\text{S II}]/\text{H}_\alpha) - 0.32) + 1.30 \quad (3.4)$$

$$\log([\text{O III}]/\text{H}_\beta) = 0.73/(\log([\text{O I}]/\text{H}_\alpha) + 0.59) + 1.33 \quad (3.5)$$

These regions will enable the identification of the source of ionisation due to ongoing star formation, as seen within jellyfish galaxies observed during the GASP survey, or something more akin to the emission seen in galaxies such as those shown in Fossati et al. (2016) which is more shock driven. Kauffmann et al. (2003) investigated three additional lines which are to be used in conjunction with

those already posed by Kewley & Dopita (2002) which could separate SF and AGN (Seyferts and LINERs) galaxies. These lines are represented through the following equations:

$$\log([\text{O III}]/\text{H}\beta) = 0.61/(\log([\text{N II}]/\text{H}\alpha) - 0.05) + 1.3 \quad (3.6)$$

$$\log([\text{O III}]/\text{H}\beta) = 1.89 \log([\text{S II}]/\text{H}\alpha) + 0.76 \quad (3.7)$$

$$\log([\text{O III}]/\text{H}\beta) = 1.18 \log([\text{O I}]/\text{H}\alpha) + 1.30 \quad (3.8)$$

Using the higher S/N regions of composite spectra, emission line ratios are created from each section as follows: $[\text{O III}]/\text{H}\beta$, $[\text{N II}]/\text{H}\alpha$, $[\text{S II}]/\text{H}\alpha$, and $[\text{O I}]/\text{H}\alpha$. These are displayed through BPT plots in Figure 3.11, where black points represent the combined region results with errors within galaxy 9011900084 (top row) and 9011900166 (bottom row). All individual spaxels within the region specified by $[\text{N II}] \text{ S/N} > 3$ are shown within as points with shapes revealing their region location (as shown within the plot key) and colour weights indicating the σ_{gas} for their corresponding spaxel. Each BPT plot contains the corresponding limit lines expressed within Equations 3.3 to 3.8, assisting with the identification of the ionisation source within each region.

For galaxy 9011900084 (top row), from the left hand panel it is clear that the central region of the galaxy contain a composite mix of gas being ionised by ongoing star formation, as well as gas that is being ionised by a non-SF source such as shocks, LINERs, or AGN. This is complicated by projection effects: a mixture of gas ionised by SF along with non-SF ionised gas along the same sight line will produce composite line ratios. The remaining regions are being ionised by a non-SF source. Within the error ranges the outer tail, inner tail, front and side regions from the right hand panel lie within regions occupied by LINER-type emission.

For galaxy 9011900166 (bottom row), from the left hand panel it is clear that the outer tail regions are being ionised by non-SF sources. The inner tail error boundaries express the possibility of it being ionised by a composite of SF and non-SF sources, along with the front region of the galaxy. Central and side regions are experiencing ionisation due to exclusively SF, however, the front region resides on the boundary towards containing ionisation sources due to non-SF. Lastly, the central and right hand panels reveal the outer tail region, and the transitioning inner tail region, as containing LINER properties.

Overall, all regions within each galaxy contain relatively similar ionisation sources. As the central regions of the galaxies still undergo ionisation by either entirely SF or a combination with a non-SF source, the outer tail regions experience ionisation by exclusively non-SF sources. The mechanism responsible for the ionisation of the gas is likely associated with shocks or interactions with the ICM,

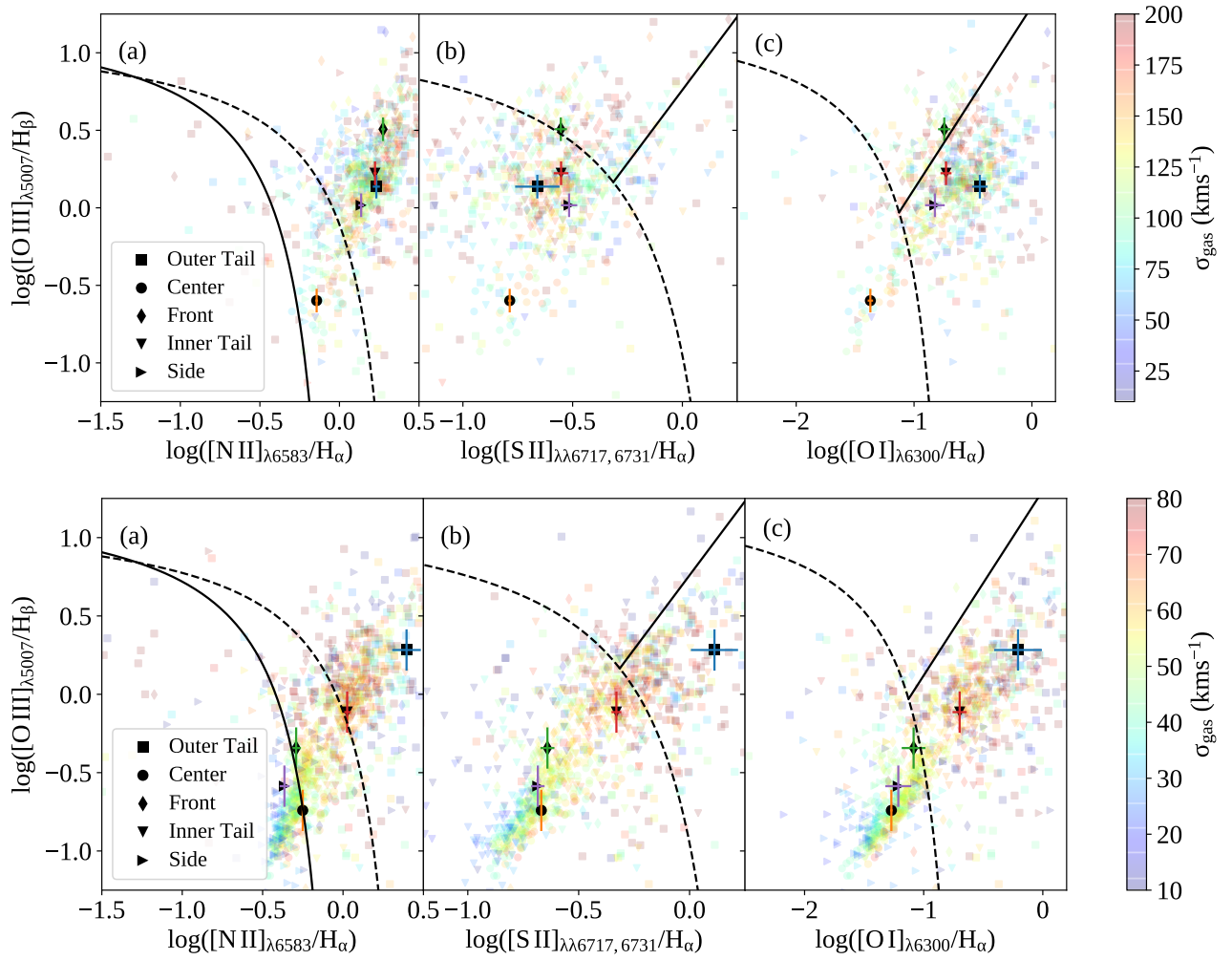


FIGURE 3.11: This figure contains three BPT emission line ratio diagnostic diagrams which assist with the classification of galaxies 9011900084 (top row) and 9011900166 (bottom row). The dashed black curves in all three show the Kewley extreme starburst definition, the solid curve in (a) shows the Kauffmann empirical relation, and the solid lines in (b) and (c) show the LINER/AGN divisions. Background coloured points represent individual spaxel results within one of the selected regions within the galaxy, as indicated through its point shape. The colour weights signify the Velocity Dispersion intensity for that specific spaxel. The results from combining spectra within each individual regions and performing a pPXF fit to each combined region is shown through each black point, where the shape indicates the same regions as the coloured points.

as observed in other systems (Merluzzi et al., 2013; Fossati et al., 2016; Boselli et al., 2019; Ramatsoku et al., 2019).

Region	$F(\text{H}\beta) / 10^{-16}$	$F([\text{O III}]) / 10^{-16}$	$F([\text{O I}]) / 10^{-16}$	$F([\text{N II}]) / 10^{-16}$	$F(\text{H}\alpha) / 10^{-16}$	$F([\text{S II}]) / 10^{-16}$
Outer Tail	2.2±0.5	3.0±0.5	2.2±0.3	10.5±0.5	6.2±0.8	2.3±0.6
Centre	57.2±0.3	14.4±0.3	7.0±0.4	118.2±2.2	164.5±2.2	48.0±0.9
Front	2.5±0.2	8.0±0.2	1.3±0.1.6	13.5±0.4	7.2±0.3	3.5±0.3
Inner Tail	4.6±0.3	7.6±0.3	2.4±0.3	21.5±0.5	12.9±0.4	6.1±0.5
Side	5.7±0.5	5.9±0.6	2.5±0.5	22.4±0.9	16.4±0.6	8.5±0.9

Region	$V_{gas} \pm \sigma$	$\sigma_{gas} \pm \sigma$
Outer Tail	-55.2±3.8	166.5±3.9
Centre	57.3±1.9	147.0±1.7
Front	34.6±1.5	139.9±1.7
Inner Tail	-48.7±2.1	154.2±1.8
Side	-36.0±3.0	169.7±2.8

TABLE 3.2: Values for the integrated flux –in units of $[\text{erg cm}^{-2} \text{s}^{-1}]$ per 0.6" pixel–, V_{gas} and σ_{gas} for individual regions in 9011900084 as labelled in Figure 3.9.

Region	$F(\text{H}\beta) / 10^{-16}$	$F([\text{O III}]) / 10^{-16}$	$F([\text{O I}]) / 10^{-16}$	$F([\text{N III}]) / 10^{-16}$	$F(\text{H}\alpha) / 10^{-16}$	$F([\text{S II}]) / 10^{-16}$
Outer Tail	0.9±0.6	1.6±0.5	1.4±0.6	5.6±1.2	2.3±1.1	5.0±1.7
Centre	84.0±0.4	15.3±0.4	13.0±0.3	136.7±1.3	243.4±1.3	89.0±0.7
Front	1.9±0.1	0.9±0.1	0.5±0.1	2.8±0.2	5.5±0.2	2.2±0.2
Inner Tail	2.8±0.2	2.2±0.2	1.6±0.2	8.5±0.4	8.0±0.4	6.4±0.4
Side	4.7±0.2	1.2±0.2	0.8±0.2	5.8±0.4	13.3±0.4	4.8±0.4

Region	$V_{gas} \pm \sigma$	$\sigma_{gas} \pm \sigma$
Outer Tail	25.4±12.3	56.6±18.1
Centre	37.8±0.4	64.8±0.5
Front	74.4±1.6	54.6±2.5
Inner Tail	64.3±2.0	58.6±2.7
Side	15.4±2.1	62.5±2.7

TABLE 3.3: Values for the integrated flux –in units of $[\text{erg cm}^{-2} \text{s}^{-1}]$ per 0.6" pixel–, V_{gas} and σ_{gas} for individual regions in 9011900166 as labelled in Figure 3.10.

Discussion

The primary drivers of this study were to initially identify evidence of environmental interactions within these galaxies, through investigating emission features, and to identify their ionisation source. Due to features observed which extend beyond the stellar disk, direction of motion along the plane of sight is also able to be inferred. Therefore, through analysing the results obtained within Section 3.2, a more accurate understanding of processes contributing to environmentally driven evolution is achieved.

4.1 Evidence for Ram Pressure Stripping

Existing evidence for galaxies 9011900084 and 9011900166 presented by Owers et al. (2019) infer the galaxies as central SF galaxies which are currently being quenched due to RPS attributed to their infall close to pericentre. Evidence provided was indirect due to the limited FoV investigated. Using the larger FoV provided by KOALA, a more direct investigation into determining the presence of RPS through one-sided tails of gas is achieved. Investigations into the evolution of galaxies through RPS have also previously been investigated within surveys such as VESTIGE (Boselli et al., 2018a), MUSE (Fumagalli et al., 2014), ACCESS (Haines et al., 2011), and GASP (Poggianti et al., 2017c), which reveal the presence of jellyfish galaxies due to their gas tail structures which contain SF.

Through investigating flux maps of both galaxies, [N II] emission features are observed extending past the stellar disk to one side of the galaxy. Previous work indicates that the presence of these tail features infer the presence of RPS (Kapferer et al., 2009). Therefore, for galaxies upon their first infall into the central region of the cluster, the primary environmental effect which is impacting the SF within the galaxy is due to RPS.

4.2 Direction of Motion

From the investigation of H δ -strong galaxies (HDSGs) within the SAMI galaxy survey (Owers et al., 2019), positions and line of sight velocities galaxies were used to infer that the galaxies are consistent with an infalling population which was accreted within $0.5 R_{200}$ within the last 1 Gyr. However, uncertainties arose surrounding the location of the galaxies in relation to pericentre, which was achieved through investigating the gas tail extension direction in relation to the centre of cluster direction. The Smith et al. (2010) investigation of UV galaxy tails in the Coma cluster found that the majority of galaxy tails (11/13 cases) pointed away from the cluster centre, indicating that the galaxies are likely observed on their way to pericentre.

Within this thesis we attempt to infer pre- or post-pericentre by estimating the direction of motion in the plane of the sky, which adds an extra observable that was not previously possible. This inference assumes that the tail orientation is a direct consequence of the ram-pressure experienced by a galaxy moving through a static ICM. Smith et al. (2010) was able to draw their conclusions due to the consistencies between galaxies within their larger sample size. Here, it is found that for both galaxies the tail orientation is not directed away from the cluster centre. The observations in Section 3.2.1 and in Figure 4.1 show the tails make angles of roughly 0° and 90° with the vector pointing towards the cluster centre for 9011900084 and 9011900166, respectively. While we cannot currently know the exact location of the galaxies along our line of sight, the contrasting orientation of the tails compared with those seen in Coma (Smith et al., 2010; Yagi et al., 2010) indicate that these galaxies may be observed later in their infall evolution. It is speculated that 9011900084 is at post-pericentre heading towards apocentre while 9011900166 is very close to pericentre. If 9011900166 is assumed to be at pericentre, it therefore has a relatively large impact parameter (approximately its distance from the cluster centre) which may account to why it has more ongoing star formation than 9011900084, which at post-pericentre has a lesser impact parameter. This indicates that 9011900084 may have experienced stronger ram-pressure for a more extended period when compared with 9011900166.

4.3 Composition

From the BPT plots, regions which are ionising due to SF or non-SF sources, such as shocks, LINERs, Seyferts or AGN, are identified. As seen in the top row of Figure 3.11 for galaxy 9011900084, the central region has line ratios suggesting a composite of SF and non-SF ionising sources. The other regions, as labelled in Figure 3.9, are ionised by non-SF sources such as shocks. This is comparable

to galaxy 9011900166 seen the bottom row of Figure 3.11, where the emission within entire galaxy disk is dominated by photo-ionisation due to young stars.

Gas tail features, representing the stripping of the ISM gas and dust from the galaxy, are not observed to be SF through an investigation into the $[\text{N II}]/\text{H}\alpha$ flux regions within the BPT plots (Figure 3.11). The absence of ionisation due to ongoing SF in these tail structures indicates that these galaxies are different from jellyfish galaxies, which show evidence for ongoing star formation in their tails. However, we may be unable to resolve the H II regions in our data because of the low S/N in the per-spaxel data, and the relatively large seeing (see Richards et al., 2014, for an extended discussion of observing H II regions in SAMI galaxies). Therefore, we don't see evidence for star formation. Follow-up with MUSE on the Very Large Telescope (VLT) in its adaptive optics mode would allow much deeper, higher resolution observations that would reveal ongoing star formation.

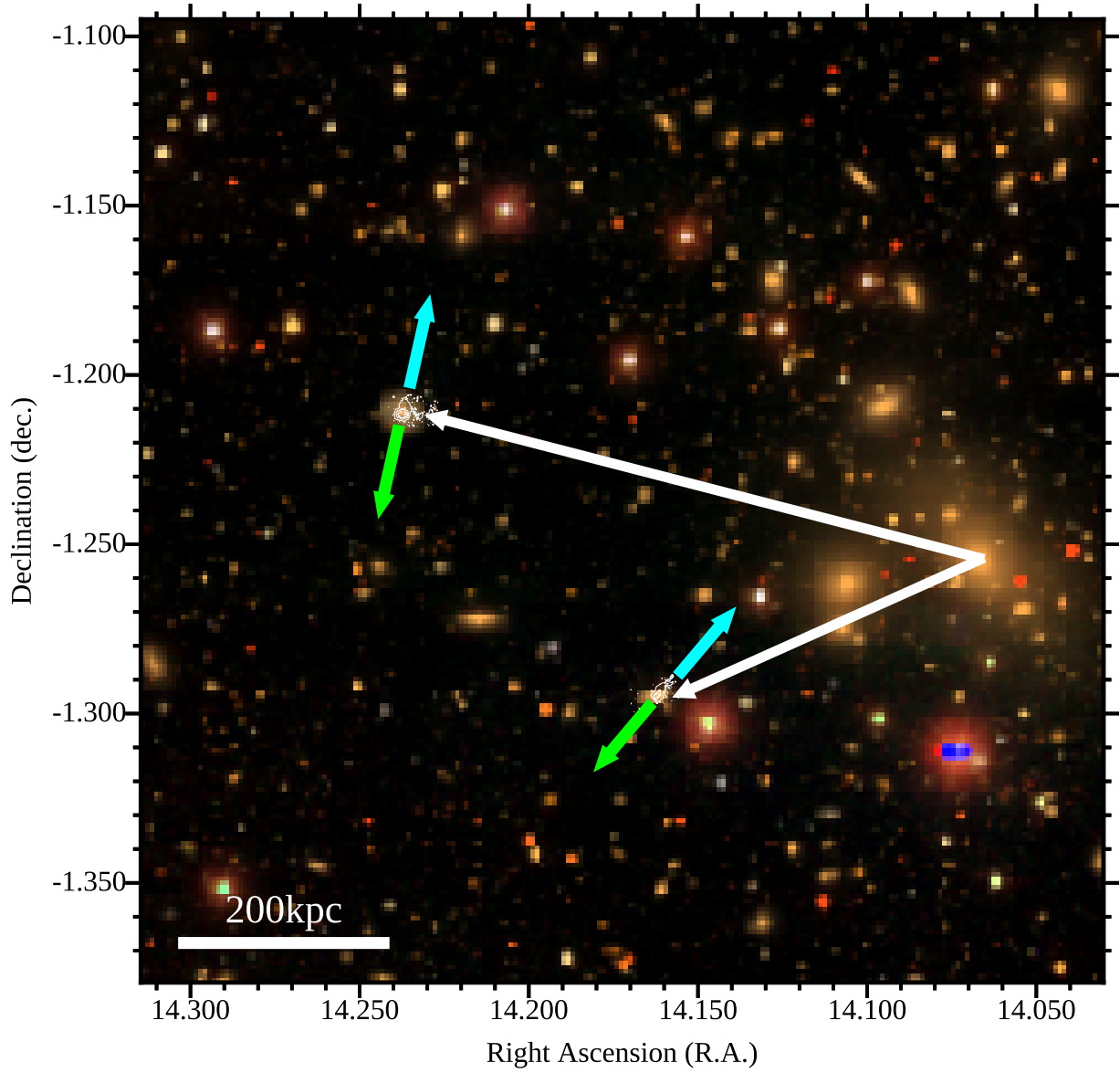


FIGURE 4.1: This figure reveals the direction of motion of the two investigated galaxies within the cluster. The image is an SDSS image with each galaxy overlapped with a white contour of the [NII] flux map lines at $S/N=[3, 25, 55]$. Cyan lines symbolise the direction in which the galaxies have travelled and the green lines infer the direction of motion of the galaxies in the plane of the sky. White lines indicate the direction of each galaxy from the centre of the galaxy cluster. North is towards the top of the page and West is towards the right.

Conclusion

5.1 Summary

The resolved data cubes produced from KOALA+AAOmega have enabled an investigation into the open questions surrounding the evolution of galaxies over time and the effect environment has on this process. Galaxies 9011900084 and 9011900166 within the cluster Abell 119 were selected to be investigated within this thesis due to their previous analysis by Owers et al. (2019). In Owers et al. (2019), it was hypothesised that the star formation (SF) in these galaxies was being quenched in an outside-in manner due to the effects of ram-pressure stripping on the first passage through the cluster cores. The natural outcome of ram-pressure stripping is one-sided gas tails that have been stripped from the galaxy. These tails can manifest through radio observation (HI), X-ray observation, pockets of star formation (indicating jellyfish galaxies), and also as faint diffuse emission in the optical due to ionised gas. The wide field of view provided by the KOALA IFU was used to search for evidence of these stripped tails, as has been observed previously within the Virgo (Boselli et al., 2018b; Poggianti et al., 2017c), Coma (Smith et al., 2010), and Norma (Fossati et al., 2016) clusters containing ram-pressure affected galaxies.

The key results found in this study are summarised as follows:

1. The initial key result is the detection of the one-sided, extended, faint emission due to ionised gas. This strongly indicates the presence of a tail of gas that has been stripped from the galaxy by ram-pressure as the galaxy hurtles through the intracluster medium (ICM).
2. The orientation of the tails infers the direction of motion in the plane of the sky. As seen in Figure 4.1, the tail feature direction with respect to the cluster centre reveal 9011900084 as post-pericentre heading in a South-East direction, where 9011900166 is assumed to be in its

closest approach to pericentre and heading in a more easterly direction. These results are in contrast to previous results in the Coma cluster, where the majority of tails are observed to point away from the cluster centre (Smith et al., 2010).

3. Obtaining combined spectra for regions within each galaxy produced higher S/N results compared to their individual spaxel counterparts, enabling the investigation of features which were previously too weak to detect. BPT diagrams are used to understand the ionising source for any emission in the tails. Considering the tail features observed associated with both galaxies, the analysis of emission line ratios demonstrated high values of $[\text{N II}]/\text{H}_\alpha$ compared to the regions within the stellar disk. Therefore, photo-ionisation due to ongoing star formation is not the ionising mechanism responsible for the emission observed in the tails. Within the stellar disk of galaxy 9011900084, only the central region experiences a composite ionisation of both SF and non-SF sources. The remaining regions reside within the LINER portion of the BPT diagram. This is similar to galaxy 9011900166 as the tail features are ionised through non-SF LINER sources, however emission within the galaxy disk is dominated by photo-ionisation by young stars.

Therefore, the results presented within this thesis are consistent with the ram-pressure stripping scenario posed by Owers et al. (2019). The results indicate that 9011900084 and 9011900166 may be observed after, or very close to, pericentric passage, although this interpretation is complicated by projection effects. Shocks resulting from the interaction between the galaxy and the ICM could be responsible for ionising the gas in the investigated galaxies tails. However, we do not see evidence for ionisation due to ongoing star formation in the tails, as seen in jellyfish galaxies (Poggianti et al., 2019).

5.2 Future Work

This thesis utilises IFU observations to identify the regions which are ionised due to either SF or non-SF sources, although does not explicitly recognise these sources with certainty. Therefore, further study is required to ensure the observation of gas tails within X-ray, H I, cold molecular gas, and ionised gas regions for these galaxies and obtain a greater understanding of these ionisation sources. Considering current instruments, it is extremely difficult to perform observations where the HI morphologies of the tails could be observed at this redshift. Through utilising the increased sensitivity and resolution

of instruments such as the upcoming Square Kilometre Array (SKA, Norris et al. 2013), this analysis is possible. Performing a comparisons between stellar and gas kinematics is also possible. This will further verify environmental perturbation events responsible for these ionisation sources.

The best-fit models for the stellar continuum derived in Section 3.1.2 of this thesis allowed for robust measurements of the emission lines. However, these best-fitting models also encode information on the underlying stellar populations in the galaxies, which could be used to constrain star formation histories. An interesting future avenue would be to explore the spatially-resolved stellar population properties of the galaxies, and to compare them with predictions from models of ram-pressure stripping. This will help to constrain the history of stripping in these galaxies.

In order to understand whether the majority of the HDSGs seen in Owers et al. (2019) are pre- or post-pericentre, further work is required to perform the analysis presented within this thesis on a larger galaxy sample. Therefore, by following up the full 8 cluster sample presented by Owers et al. (2019), a more systematic search for tails could be performed. This will provide more stringent tests of the RPS scenario, and to also confirm the pre/post pericentre question using a more statistically significant sample, as performed by Smith et al. (2010).

References

- Abell G. O., Cormin JR H. G., Olowin R. P., 1989, The Astrophysical Journal Supplement Series, 70, 1
- Allen J. T., et al., 2015, Monthly Notices of the Royal Astronomical Society, 446, 1567
- Baldwin J., Phillips M., Terlevich R., 1981, Astronomical Society of the Pacific, 93, 5
- Barnes J. E., Hernquist L., 1996, The Astronomical Journal, 471, 115
- Bing L., et al., 2019, Monthly Notices of the Royal Astronomical Society, 482, 194
- Boselli A., Gavazzi G., 2006, Publications of the Astronomical Society of the Pacific, 118, 517
- Boselli A., et al., 2016, Astronomy & Astrophysics, 587, A68
- Boselli A., et al., 2018a, Astronomy and Astrophysics, 614
- Boselli A., et al., 2018b, Astronomy & Astrophysics, 620, A164
- Boselli A., et al., 2019, Astronomy and Astrophysics, 623, 1
- Bryant J. J., et al., 2015, Monthly Notices of the Royal Astronomical Society, 447, 2857
- Butcher H., Oemler A., 1978, The Astronomical Journal, 219, 18
- Butcher H., Oemler A., 1984, Astronomical Journal, 285, 426
- Byrd G., Valtonen M., 1990, The Astronomical Journal, 350, 89
- Cappellari M., 2009, pp 1–16
- Cappellari M., 2017, Monthly Notices of the Royal Astronomical Society, 466, 798
- Cappellari M., Emsellem E., 2004, The Astronomical Society of the Pacific, 116, 138
- Cid Fernandes R., Stasińska G., Schlickmann M. S., Mateus A., Vale Asari N., Schoenell W., Sodré L., 2010, Monthly Notices of the Royal Astronomical Society, 403, 1036

- Coenda V., Martínez H. J., Muriel H., 2018, *Monthly Notices of the Royal Astronomical Society*, 473, 5617
- Cora S. A., et al., 2018, *Monthly Notices of the Royal Astronomical Society*, 479, 2
- Croom S., Saunders W., Heald R., 2004, *AAO Newslett.*, 106, 12
- Croom S. M., et al., 2012, *Monthly Notices of the Royal Astronomical Society*, 421, 872
- Croton D. J., et al., 2006, *Monthly Notices of the Royal Astronomical Society*, 365, 11
- Dressler A., 1980, *Astrophysical Journal*, 236, 351
- Dressler A., Gunn J. E., 1983, *The Astronomical Journal*, 270, 7
- Ellis S. C., et al., 2012, *Proc. SPIE*, 8446, 84460V
- Faber S. M., et al., 2007, *The Astrophysical Journal*, 665, 265
- Fang J. J., Faber S. M., Salim S., Graves G. J., Rich R. M., 2012, *Astrophysical Journal*, 761, 23
- Fossati M., Fumagalli M., Boselli A., Gavazzi G., Sun M., Wilman D. J., 2016, *Monthly Notices of the Royal Astronomical Society*, 455, 2028
- Fumagalli M., Fossati M., Hau G. K., Gavazzi G., Bower R., Sun M., Boselli A., 2014, *Monthly Notices of the Royal Astronomical Society*, 445, 4335
- George K., et al., 2019, *Monthly Notices of the Royal Astronomical Society*, 487, 3102
- Gunn J., Gott J. R., 1972, *Astrophysical Journal*, 176, 1
- Haines C. P., Busarello G., Merluzzi P., Smith R. J., Raychaudhury S., Mercurio A., Smith G. P., 2011, *Monthly Notices of the Royal Astronomical Society*, 412, 127
- Harrison C. M., Alexander D. M., Mullaney J. R., Swinbank A. M., 2014, *Monthly Notices of the Royal Astronomical Society*, 441, 3306
- Ho I.-T., et al., 2014, *Monthly Notices of the Royal Astronomical Society*, 444, 3894–3910
- Hubble E., 1926, *Astrophysical Journal*, 64, 321
- Husemann B., Kamann S., García-Benito R., Sandin C., Husemann B., Mast D., Sánchez S. F., 2012, *Astronomy & Astrophysics*, 545, A137

- Kapferer W., Sluka C., Schindler S., Ferrari C., Ziegler B., 2009, *Astronomy and Astrophysics*, 499, 87
- Kauffmann G., White S. D. M., Guiderdoni B., 1993, *Monthly Notices of the Royal Astronomical Society*, 264, 201
- Kauffmann G., et al., 2003, *Monthly Notices of the Royal Astronomical Society*, 346, 1055
- Kewley L. J., Dopita M. A., 2002, *The Astrophysical Journal Supplement Series*, 142, 35
- Kewley L. J., Groves B., Kauffmann G., Heckman T., 2006, *Monthly Notices of the Royal Astronomical Society*, 372, 961
- Larson R. B., Tinsley B. M., Caldwell C. N., 1980, *The Astrophysical Journal*, 237, 692
- Lenz D. D., Ayres T. R., 1992, *Astronomical Society of the Pacific*, 104, 1104
- Madau P., 1995, *Astronomical Journal*, 441, 18
- Merluzzi P., et al., 2013, *Monthly Notices of the Royal Astronomical Society*, 429, 1747
- Merluzzi P., Busarello G., Dopita M. A., Haines C. P., Steihauser D., Bourdin H., Mazzotta P., 2016, *Monthly Notices of the Royal Astronomical Society*, 460, 3345
- Moore B., Katz N., Lake G., Dressler A., Oemler A., 1996, *Nature*, 379, 613
- Norris R. P., et al., 2013, *Publications of the Astronomical Society of Australia*, 30
- Owers M. S., et al., 2017, *Monthly Notices of the Royal Astronomical Society*, 468, 1824
- Owers M. S., et al., 2019, *The Astrophysical Journal*, 873, 52
- Poggianti B. M., et al., 2009, *Astrophysical Journal*, 693, 112
- Poggianti B. M., et al., 2017a, *Nature*, 548, 304
- Poggianti B. M., et al., 2017b, *The Astrophysical Journal*, 844, 1
- Poggianti B. M., et al., 2017c, *The Astrophysical Journal*, 844, 48
- Poggianti B. M., et al., 2019, *Monthly Notices of the Royal Astronomical Society*, 482, 4466

- Radovich M., Poggianti B., Jaffé Y. L., Moretti A., Bettoni D., Gullieuszik M., Vulcani B., Fritz J., 2019, *Monthly Notices of the Royal Astronomical Society*, 486, 486
- Ramatsoku M., et al., 2019, *Monthly Notices of the Royal Astronomical Society*, 487
- Richards S. N., et al., 2014, *Monthly Notices of the Royal Astronomical Society*, 445, 1104
- Salim S., 2014, *Serbian Astronomical Journal*, 1, 1
- Saunders W., et al., 2004, in Moorwood A. F. M., Iye M., eds, Vol. 5492, *Ground-based Instrumentation for Astronomy*. SPIE, pp 389–400, doi:10.1117/12.550871, <https://doi.org/10.1117/12.550871>
- Sharp R., Birchall M. N., 2010, *Publications of the Astronomical Society of Australia*, 27, 91
- Sharp R., et al., 2006, *Ground-based and Airborne Instrumentation for Astronomy*, 6269, 62690G
- Sharp R., et al., 2015, *Monthly Notices of the Royal Astronomical Society*, 446, 1551
- Smith G. A., et al., 2004, in Moorwood A. F. M., Iye M., eds, Vol. 5492, *Ground-based Instrumentation for Astronomy*. SPIE, pp 410–420, doi:10.1117/12.551013, <https://doi.org/10.1117/12.551013>
- Smith R. J., et al., 2010, *Monthly Notices of the Royal Astronomical Society*, 408, 1417
- Snyder G. F., Cox T. J., Hayward C. C., Hernquist L., Jonsson P., 2011, *Astrophysical Journal*, 741
- Sun M., Donahue M., Voit G. M., 2007, *The Astrophysical Journal*, 671, 190
- Thilker D. A., et al., 2010, *Astrophysical Journal Letters*, 714, L171
- Toomre A., Toomre J., 1972, *The Astrophysical Journal*, 178, 623
- Trayford J. W., Theuns T., Bower R. G., Crain R. A., Lagos C. d. P., Schaller M., Schaye J., 2016, *Monthly Notices of the Royal Astronomical Society*, 460, 3925
- Trussler J., Maiolino R., Maraston C., Peng Y., Thomas D., Goddard D., Lian J., 2019, *Monthly Notices of the Royal Astronomical Society*, 31, 1
- Vazdekis A., Sánchez-Blázquez P., Falcón-Barroso J., Cenarro A. J., Beasley M. A., Cardiel N., Gorgas J., Peletier R. F., 2010, *Monthly Notices of the Royal Astronomical Society*, 404, 1639
- Vergani D., et al., 2018, *Astronomy and Astrophysics*, 509

- Vulcani B., et al., 2019, Monthly Notices of the Royal Astronomical Society, 488, 1597–1617
- Wyder T. K., et al., 2007, Astrophysical Journal, Supplement Series, 173, 293
- Yagi M., et al., 2010, Astronomical Journal, 140, 1814
- Zabludoff A. I., Zaritsky D., Lin H., Tucker D., Hashimoto Y., Shectman S. A., Oemler A., Kirshner R. P., 1996, The Astronomical Journal, 466, 104
- Zhelem R., et al., 2014, Ground-based and Airborne Instrumentation for Astronomy V, 9147, 91473K
- van Dokkum P. G., 2001, Publications of the Astronomical Society of the Pacific, 113, 1420
- van de Sande J., et al., 2017, Monthly Notices of the Royal Astronomical Society, 472, 1272